G. B. Crosta · C. di Prisco · P. Frattini · G. Frigerio · R. Castellanza · F. Agliardi

Chasing a complete understanding of the triggering mechanisms of a large rapidly evolving rockslide

Abstract Rockslides in alpine areas can reach large volumes and, owing to their position along slopes, can either undergo large and rapid evolution originating large rock avalanches or can decelerate and stabilize. As a consequence, in particular when located within large deep-seated deformations, this type of instability requires accurate observation and monitoring. In this paper, the case study of the La Saxe rockslide (ca. 8×10^6 m³), located within a deep-seated deformation, undergoing a major phase of acceleration in the last decade and exposing the valley bottom to a high risk, is discussed. To reach a more complete understanding of the process, in the last 3 years, an intense investigation program has been developed. Boreholes have been drilled, logged, and instrumented (open-pipe piezometers, borehole wire extensometers, inclinometric casings) to assess the landslide volume, the rate of displacement at depth, and the water pressure. Displacement monitoring has been undertaken with optical targets, a GPS network, a ground-based interferometer, and four differential multi-parametric borehole probes. A clear seasonal acceleration is observed related to snow melting periods. Deep displacements are clearly localized at specific depths. The analysis of the piezometric and snowmelt data and the calibration of a 1D block model allows the forecast of the expected displacements. To this purpose, a 1D pseudo-dynamic visco-plastic approach, based on Perzyna's theory, has been developed. The viscous nucleus has been assumed to be bi-linear: in one case, irreversible deformations develop uniquely for positive yield function values; in a more general case, visco-plastic deformations develop even for negative values. The model has been calibrated and subsequently validated on a long temporal series of monitoring data, and it seems reliable for simulating the in situ data. A 3D simplified approach is suggested by subdividing the landslide mass into distinct interacting blocks.

Keywords Mont de La Saxe rockslide · Monitoring · GB-Insar · Displacement forecast · Visco plastic model · Slope hydrology

Introduction

Rockslides undergoing rapid changes in behavior represent a major risk in alpine areas, requiring careful characterization and monitoring, both for civil protection activities and to plan slope stabilization strategies. In particular, these instabilities can follow a phase of very slow and almost imperceptible movement, after which seasonal rapid accelerations or collapse can take place. The analysis of such instabilities, subject to continuous slow movements and intermittent stages of slowing and rapidly (occasional or seasonal) accelerating motion, is a challenging issue in geological and geotechnical problems. These types of landslides can occur high on the valley and mountain flanks causing risk over large areas along the valley bottom, and can rapidly evolve into a relatively short time due to the progressive failure of the rock mass or due to an external agent which can trigger instability (Gillon and Hancox 1992; Gillon et al. 1992; Crosta and Agliardi 2003; Glastonbury and Fell 2010; Helmstetter and Garambois 2010; Nishii et al. 2013).

Many translational or roto-translational landslides occurring in Northern Italy (Crosta et al. 2006) are characterized by velocities on the order of few centimeters per year. Usually, this behavior does not result in sudden and unexpected failures; nevertheless, it can substantially impact the stability of infrastructures (roads, tunnels, etc.) and civil buildings. Several case studies of large rockslides have been presented in the literature (Crosta and Agliardi 2002; Casagli et al. 2010; Ganerød et al. 2008; Chigira 2005; Helmstetter and Garambois 2010; Zangerl et al. 2010; Grøneng et al. 2011; Gischig et al. 2011; Agliardi et al. 2012) showing dependence of displacement rate on seasonal and annual changes of external factors [rainfall, snowmelt (Moore and Imrie 1995; Nishii et al. 2013), temperature oscillations] or on human actions (e.g., impounding of landslide toe by artificial lakes; Macfarlane 2009; Macfarlane et al. 1992a, b; Mansour et al. 2011).

The study of the triggering of such rockslides can be focused on either the initial failure or the successive reactivations driven by either meteo-climatic events or other perturbations. Displacements are generally triggered by hydrologic factors and a correlation between groundwater level oscillations and slope movements has been observed (Angeli et al. 1996; Butterfield 2000; Lollino et al. 2006; Corominas et al. 2005; Gottardi and Butterfield 2001; Helmstetter and Garambois 2010; Ranalli et al. 2010). This seasonal dynamic behavior generally shows a delay between perturbation (e.g., groundwater recharge and increase in water table level) and system reaction (e.g., increase in displacement rate). Therefore, it can be correlated with a typical viscous response inducing a permanent—and time delayed—deformation of the unstable mass. These rockslides can reach very large volumes making their stabilization technically difficult or prohibitive in terms of both sustainable costs and logistics. To develop a good understanding of this behavior, monitoring systems are set up with the aim of providing a continuous description of the movement evolution and estimating the expected displacement or eventually the collapse time. The monitoring data should be as complete as possible, to allow the understanding of landslide activity and the sensitivity to external perturbations, the prediction of future evolution, the estimate of expected displacements and accelerations, and the definition of threshold values to be implemented within Early Warning Systems (EWS).

Furthermore, most of these landslides are complex phenomena characterized by an evolution that can be different for individual sectors within the landslide, each at a different evolutionary step, and that can evolve with time through a progressive failure. In order to fulfill such a scope, a monitoring network should include both surface and subsurface instrumentation (Eberhardt et al. 2008), and the data needs to be interpreted by suitable methods. At the same time, these methods should be relatively simple to allow implementation within the EWS.

In the following paper, we present the case study of the Mont de La Saxe rockslide (Courmayeur, Aosta Valley, Italy) as an example of complex investigations caused by environmental and local risk

Basin	Area, km²	Basin	Area, km²	Basin	Area, km²
7	0.146	1	0.022	4	0.017
8	0.219	2	0.062	5	0.038
		3	0.006	6	0.025

——	landslide boundary		——	stream network
——	DSGSD counterscarps		•	springs
——	DSGSD scarps		▭	landslide drainage basin
·····	lineaments		▭	inferred hydrogeological basin
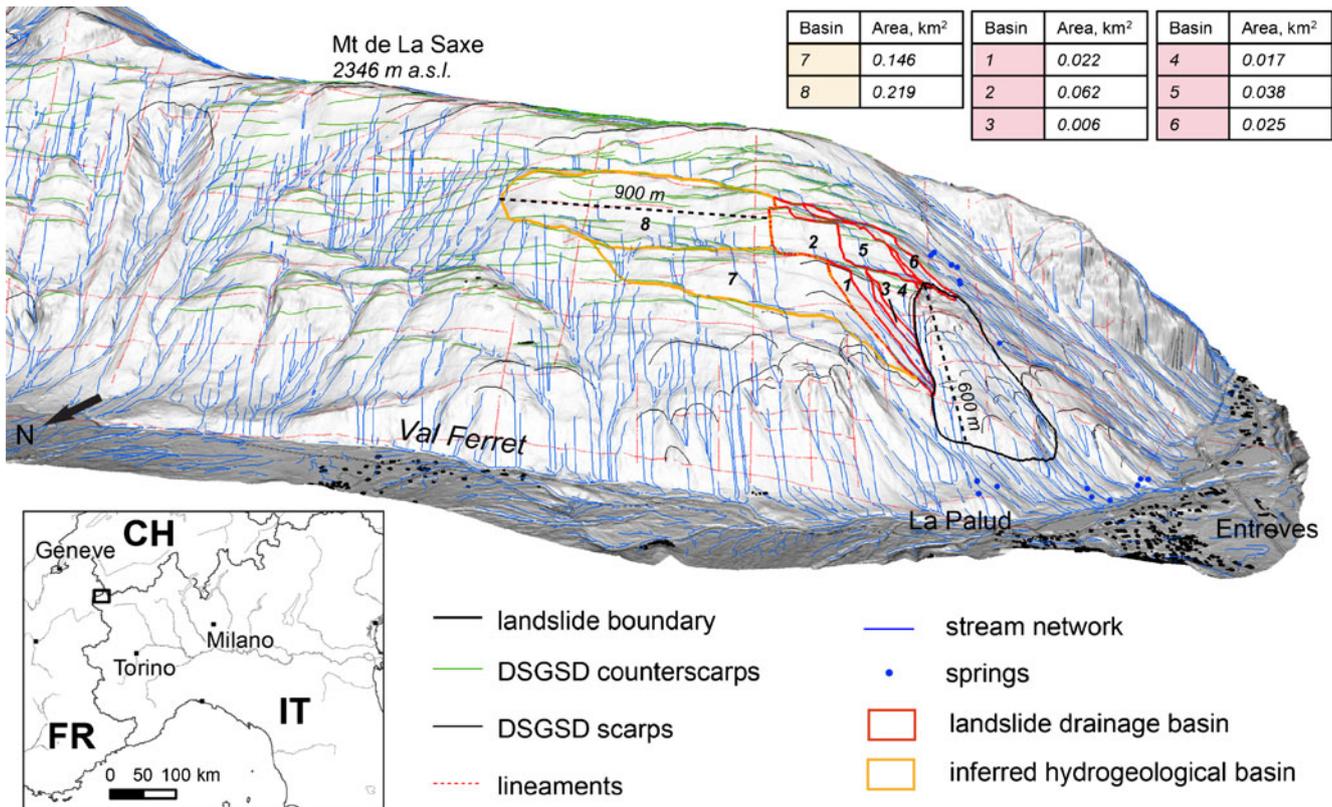
Fig. 1 Shaded 1 m × 1 m LiDAR DEM of the left hand flank of the Ferret valley. The orientation of the morphostructures and their termination close to the rockslide crown area are visible. The superficial drainage network and the small catchments directly contributing to the rockslide at different points are shown

considerations and substantial slope activity. This active rockslide generates a high consequence of failure because of its location just above Entrèves village and its proximity to the Mont Blanc highway and tunnel, to the Mont Blanc cableway, and to the access for some important tributary.

In addition to the local population, large numbers of tourists visit the area both during the winter and summer seasons. Therefore, the possible impact on the area by the potential rockslide is important both from the social and economic point of view.

The Mont de La Saxe rockslide

The Mont de La Saxe rockslide is located in an area known to be unstable for many years (Ratto et al. 2007; Broccolato, M et al. 2011a, b; Crosta et al. 2012a, b), although very little detailed information exists concerning its activity. The rockslide is located at the extreme SW termination of a deep-seated gravitational slope deformation (DSGSD), which occupies the terminal sector of the left-hand side of the Ferret Valley (Fig. 1). Here, rockslide deformations clearly displace gravitational morphostructures (scarps, counterscarps, trenches) related to the DSGSD, whose SW–NE rectilinear trend appears strongly disturbed or obliterated inside the rockslide area (Figs. 1, 2, and 3). This observation may be relevant to the definition of structural constraints for landslide geometry modeling and stability analysis setup (e.g., pre-existing occurrence of weakness zones with different physical mechanical properties with respect to the other slope sectors).

The rock slide (of about 8×10^6 m³) extends between 1,400 and 1,870 m a.s.l., over an area of about 150,000 m², with maximum horizontal length of about 550 m, maximum width of about 420 m, and average slope gradient of 37°. The upper scarp is about 200 m wide and it is characterized by a steep rock wall some tens of meters high, locally oriented along subvertical schistosity planes (Fig. 3).

Since no quantitative information was available to characterize the state of activity of this slope during the past decades, detailed multi-temporal and multi-scale analyses of available aerial photos have been undertaken. Interferometric PS-InSAR and SqueeSAR analyses (ERS1 and ERS2, from 1993 to 2000 and from 1992 to 2000 for ascending and descending mode, respectively; Radarsat, from 2003 to 2010, all performed by TeleRilevamentoEuropa) have been

Fig. 2 The left hand flank of the Ferret valley. The photo is taken from the Mt Blanc massif and shows the deep-seated gravitational slope deformation and the Mont de La Saxe rockslide, at the valley outlet above the Entrèves village
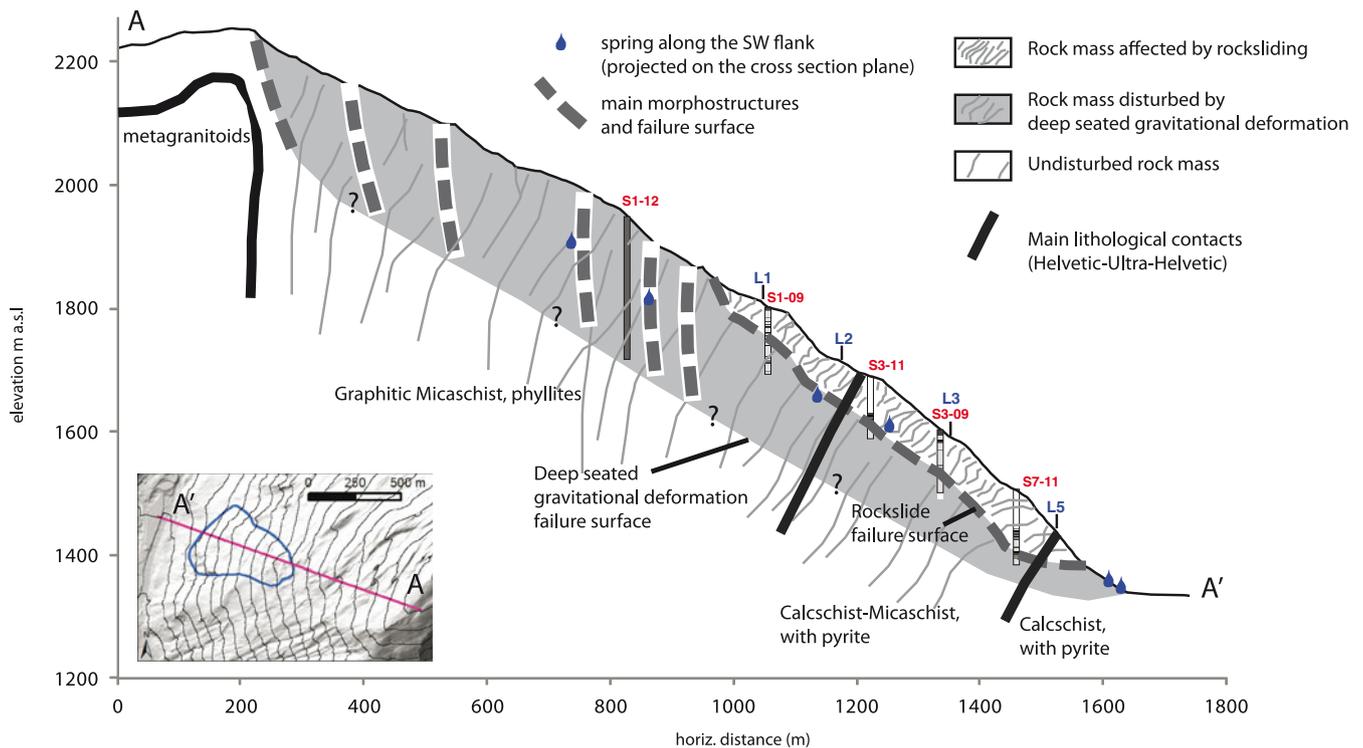
Fig. 3 Simplified cross section of the NW slope of Mt de La Saxe representing the general foliation attitude, the location of some boreholes, the rockslide failure surface as from geophysical investigations and direct inclinometric measurements, and the assumed deep-seated slope deformation surface and internal failure planes and trenches. Main lithological limits are also shown together with a zonation of the slope in sectors with different degrees of disturbance and expected hydrogeological behavior. This same cross-section has been adopted for 2D groundwater flow modeling (Fig. 12)

unable to provide information on the displacements of this unfavorably exposed NW facing valley flank (http://geonavsct.partout.it/pub/geoRelBac/). Multi-temporal analysis of aerial photos (1983, 1988, 1998, 2000, 2009) shows that in 1983, the upper slope sector was intensely vegetated and no debris scree was visible at the already existing small headscarp. Small debris flows and scree along the slope were rare in these first photos, but started to be clearly detectable in 1988, along the lower slope sector. The rockslide activity continued to develop and, on the 1998 aerial photos, the upper scarp activity became evident. Since then, the rockslide activity has increased and the occurrence of rockfalls at its toe has been observed with blocks reaching the Dora di Ferret river (2008, 2012).

Building on this basic information, several rockslide investigation activities have been undertaken since 2009 (Broccolato et al. 2011a, b; Crosta et al. 2012a), including geological and geomorphological mapping, geophysical seismic surveys, borehole drilling, in situ testing, and monitoring.

Five seismic tomography profiles have been acquired along the slope, which indicate the presence of either relaxed or fractured rock masses extending to depths up to 70–90 m, below which some relatively sound or slightly relaxed rock is present. This is suggested by the available geophysical investigation data (seismic refraction and tomography) summarized in Fig. 4.

Eighteen vertical boreholes and 11 inclined (22° to 29°) boreholes have been drilled (110 to 200 m long) in the landslide area since 2005 (see Fig. 5). The large number of boreholes is due to the complexity of the system and the need for a more complete and clear identification of the sliding surface and groundwater levels within the rockslide body. Moreover, the large displacement rate of

the rockslide has caused damage and loss of efficiency of the borehole monitoring system installed, requiring new boreholes to be drilled to continue sub-surface monitoring activities. RQD logging of boreholes and drillcores confirmed the presence of a thick (30–90 m) intensely fractured and disrupted layer located above more competent bedrock (Broccolato et al. 2011a). Foliation varies in inclination with respect to the borehole axis but mainly dips into the slope between 20° and 60°, with extremely rare subvertical orientation and seems more related to the pre-existing stratification. A borehole exceeding 200 m in depth (S1–12) has been recently drilled within one of the upper trenches, related to the DSGSD, about 70 m above the crown area (Figs. 3 and 5). Here, the rock was proved broken and extremely permeable for the entire length with only a minor presence of water (short discharge below 1 l/s). This observation is relevant to the definition of rockslide predisposing factors and provides interesting constraints to hydrogeological modeling and the effects of triggering agents.

Water or air losses were frequently observed during drilling through the upper 30 to 90 m, and no Lugeon test was feasible. Water pockets were found in two inclined drillholes, but were of short duration. Springs have been mapped and monitored periodically along the slope, the most important (with short peaks up to 10–40 l/s during the snow melting season) located high on the slope a few hundred meters S of the head scarp (see Figs. 3 and 5). The area is subjected to snow fall during the winter (average equivalent rainfall 810 mm ca., data—Mont de La Saxe meteo-station at 2,076 m a.s.l.) with a total average precipitation of about 1,470 mm (at the rock slide crown area) and a real evapo-transpiration of about 370 mm. Water infiltration in the area seems
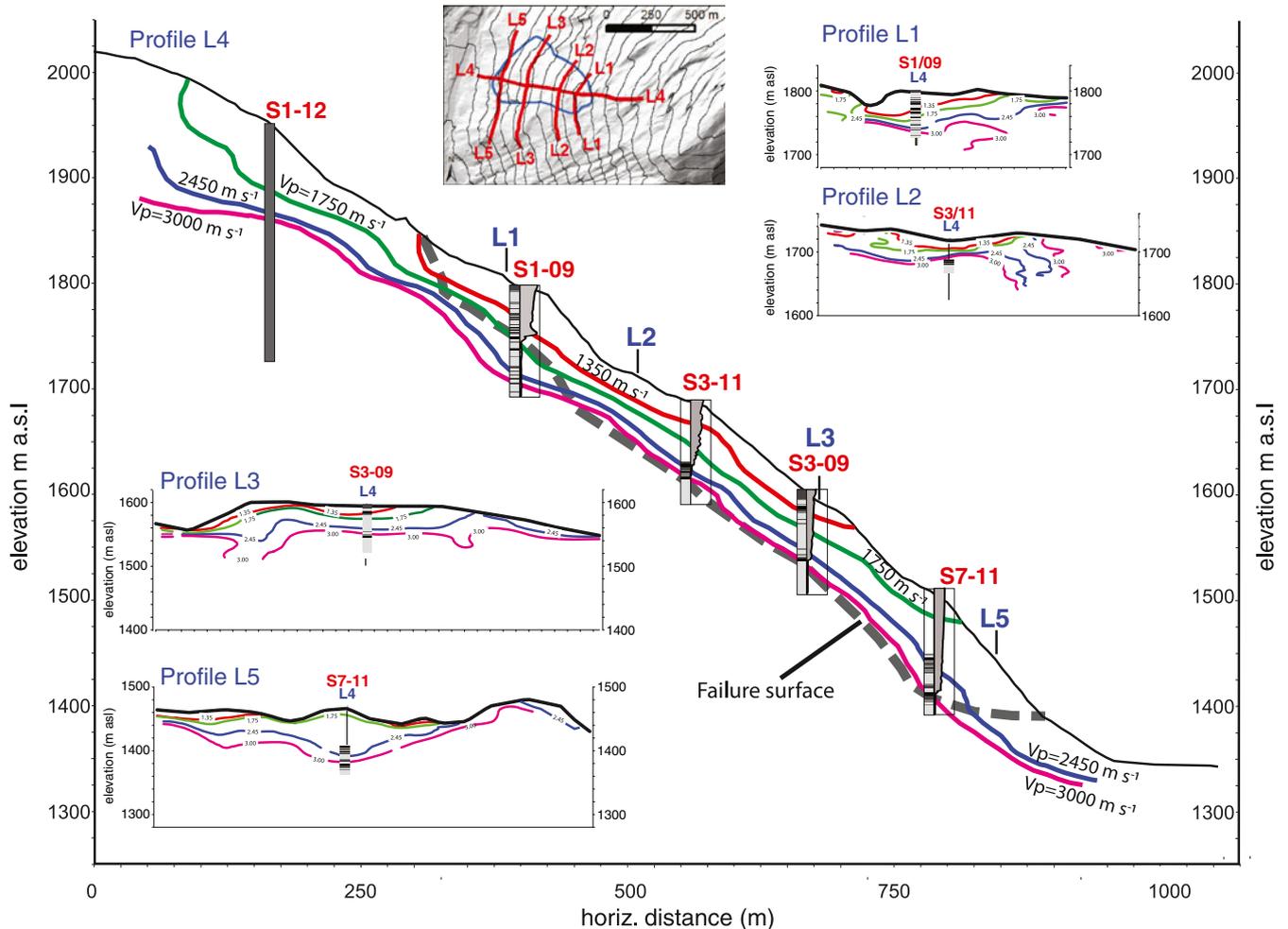
Fig. 4 Seismic refraction tomography represented in terms of isovelocity contour lines, along longitudinal and transversal investigation lines, for the lower part of the Mt de La Saxe slope. Simplified fracture intensity logs (as in Fig. 10) and measured inclinometric displacements are shown

strongly controlled by the presence of the large morphostructures and their infiltration characteristics. Morphostructures parallel to the slope direction strongly control the surface water runoff, directing it towards the rockslide crown area or favoring its percolation within the slope through the more conductive materials aligned with the trench direction (Fig. 1). Tracer tests have been performed both from the surface and from boreholes. The tests allowed us to recognize that the groundwater system is locally compartmentalized and the peak velocity from first arrivals is estimated as 10 to 20 m day^{-1}. The seepage direction transversal to the slope dip is supported by tracer testing by injection of fluorescein in borehole S1/09, which was later detected only at the springs located on the south western side of the landslide, about 100 m below the immission point. Infiltration and tracer tests within a morphostructure, few hundred meters uphill from the rockslide head scarp, showed an infiltration rate ranging between 5 and 10 l/s, which can be considered typical of these morphostructures. Furthermore, some of these morphostructures are characterized by a layered infilling with big changes in grain size, including blocks from scarp dismantling and sometimes finer levels corresponding to paleosoils. This discontinuous layering can cause also subsurface seepage in the direction of morphostructures (SW). Because of this effect, the rockslide and the head scarp area are

fed by the water drained by the morphostructures, immediately to the E and SE, making this an important controlling factor of the rockslide reactivation. The total hydrogeological area directly contributing to the rockslide has been derived from the analysis of a LiDAR DEM and sums up to 0.17 km^2 (Fig. 1). An additional area of 0.36 km^2 has been interpreted to belong to the hydrogeological basin contributing to the rockslide by percolation and preferential flow along DSGSD morphostructures during periods of high rainfall or snow melt.

The location of a deep groundwater table within the slope is controlled at a larger scale by the rockslide location at the valley outlet (see Figs. 1 and 2), where a large difference in elevation exists between the Ferret tributary valley and the main valley bottom. Here, the deep groundwater table should respond to the variations of both the secondary and main base levels (Gleeson and Manning 2008), draining water from within the Ferret valley flank. Finally, after drilling operations, most of the boreholes showed water levels at or below the depth of the sound bedrock appearance (ca. −90 m) late in the summer and during the winter.

Geological and geomorphological settings
The La Saxe rockslide is located in meta-sedimentary sequences cropping out along the left hand flank of the valley (Fig. 6). These
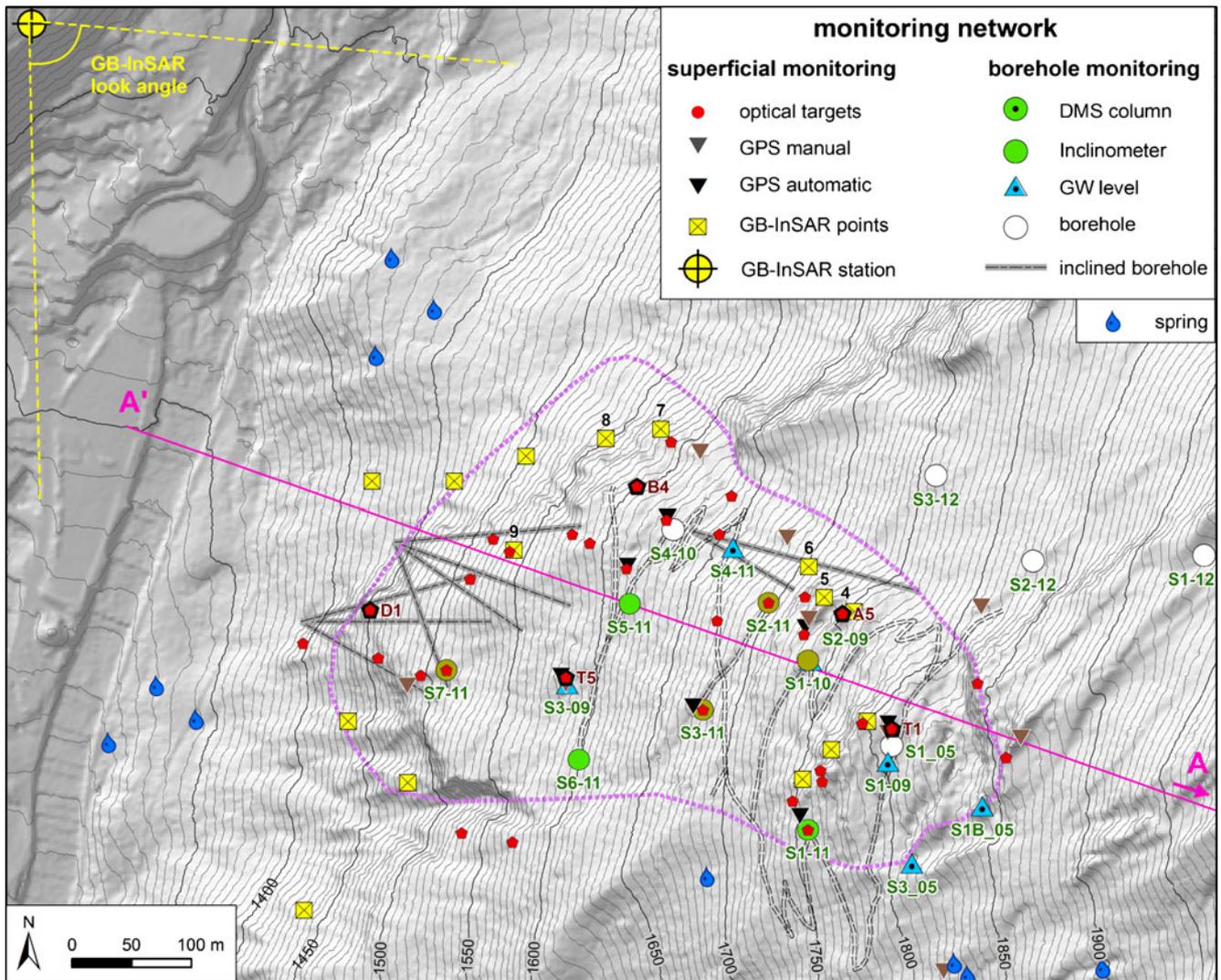
Fig. 5 Distribution of the topographic and geotechnical monitoring networks. GB-InSAR points show the position of the streaming points with continuous acquisition. DMS: multi-parametric probe; inclinometer: boreholes equipped with inclinometric casing; GW level: piezometers

rocks belong to Ultra-Helvetic basal decollement units located south of the Mt. Blanc crystalline massif and are made of very low-grade, intensely deformed Middle Jurassic meta-sedimentary sequences, including limestones and marls, argillaceous schists, black schists, micaschists, and calcschist with quartz–arenite levels (Antoine et al. 1979; Guermani and Pennacchioni 1998; Perello et al. 1999; Leloup et al. 2005). To the south, these rocks are found in tectonic contact with the Ultra Helvetic Mt. Chetif unit, made of metagranites and metarhyolites. Just a few kilometers south of the rockslide area, Ultra-Helvetic units are overthrusted along the WSW–ENE trending Frontal Penninic Thrust (PFT in Fig. 6) by low-grade meta-sedimentary sequences belonging to the External Penninic Units (Courmayeur–Sion zone). In the area affected by the rockslide, dominant black argillaceous schists prevalently dip to the SE, into the slope, with dip angles ranging between 20° and 60° (more rarely sub-vertical), due to the effect of tectonic deformation events at the outcrop scale. The rock fabric seems to be more controlled by pre-existing sedimentary features (bedding) than by the development of an axial plane foliation.

Slope morphology and superficial deposits reflect the imprint of Quaternary glaciations and subsequent readjustment by gravitational processes. The slope is extensively covered by discontinuous till deposits reworked by gravity and colluvial processes, whereas significant talus and landslide deposits are found at the slope toe. As was above mentioned, a large sector of the valley flank is affected by a DSGSD characterized by SW–NE trending morphostructures (associations of gravitational scarps and counterscarps) conditioned by persistent inherited brittle tectonic features, including subvertical, dextral strike-slip faults reactivated by slow rock slope instability. These morphostructures also exert a strong conditioning on the SW-trending pattern of superficial drainage axes, which are almost parallel to the slope direction in the upper part of the slope.

Monitoring system
As was already mentioned, some evidence of past activity along the slope has been recognized on old aerial photos, and since 2002 an evident reactivation of the phenomenon has been observed
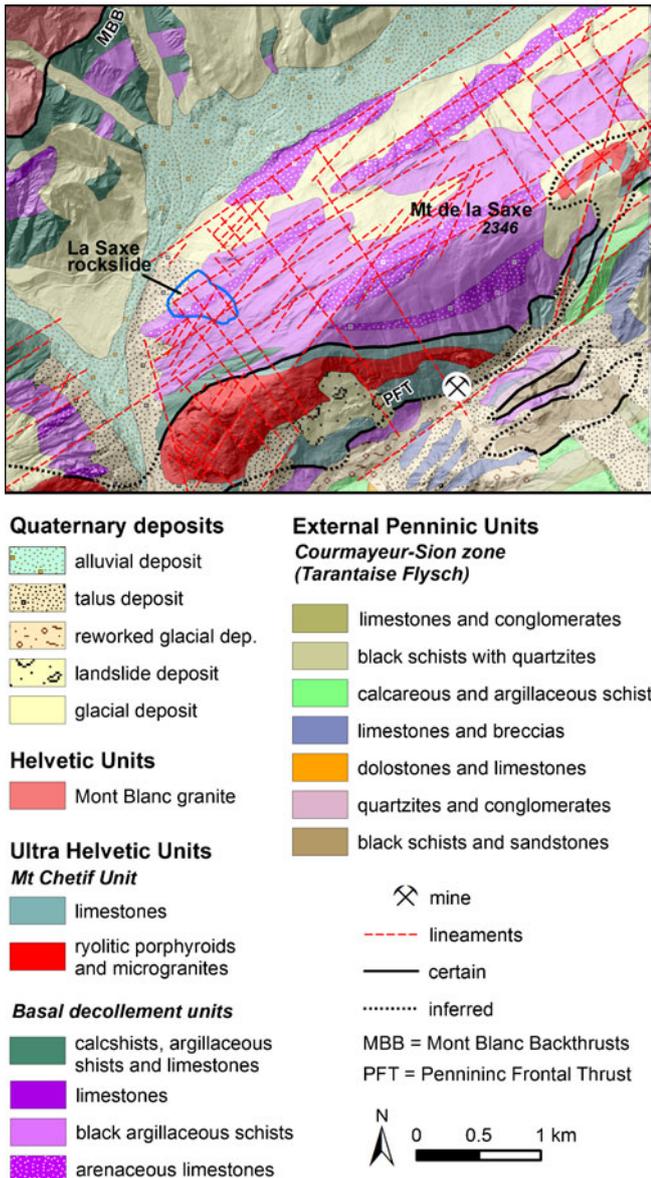
Fig. 6 Geological map of the study area as from the Geological Map of the Aosta Valley (modified from De Giusti et al. 2005). *3* Mont Blanc granite; *5* Mt Chetif sedimentary cover: Liassic limestone; *6* meta-granites, meta-rhyolites with mylonitic overprint; *7* limestones and calcschists; *8* limestones; *9* black clay schists and marly limestones; *10* calcarenites. The upside down V represents the deep-seated gravitational slope deformation along the left hand valley flank

(Broccolato et al. 2011a, b; Crosta et al. 2012a). For this reason, 15 EDM (Electronic Distance Measurement) repeated measurements of eight optical targets were carried out from two reference stations between 2002 and 2009.

In 2009, the recognized high level of risk posed by the rockslide pointed to the need for a more complete monitoring system. This has been deployed integrating different types of surface and subsurface monitoring data (both in point-like and distributed forms) to achieve a better understanding of rockslide displacement, failure mechanisms, and trigger–response relationships, and to support emergency civil protection actions.

In its present configuration and in order of deployment, the monitoring system for surficial displacements includes the following (see Fig. 5):

- 9 GPS benchmarks for periodic, manually operated measurements;
- 1 permanent GB-InSAR LisaLab[TM] system (operated by Ellegi srl);
- 5 GPS network devices for automatic continuous measurements; and
- 1 Leica TCA[TM] robotic total station, surveying 31 optical targets (four of which relocated outside the rockslide area on stable ground) hourly.

The total station is positioned on the opposite valley side, just near the LisaLab[TM] GB-InSAR system and the GPS master reference station (Fig. 4).

The GB-InSAR equipment has been operating in permanent monitoring mode since June 2009, with a synthetic aperture of 3 m. The equipment acquires radar images with a range resolution of 1.5 m, and an azimuthal resolution between 0.5 and 4 m depending on the distance from different parts of the monitored scene, ranging between 500 and 2,000 m, respectively. Radar sensor location and elevation have been selected to optimize the alignment between the radar line-of-sight and the average direction of slope displacements. The system collects and processes radar images approximately every 10 min, and provides a spatially distributed, near real-time information of landslide behavior, in the form of geo-referenced cumulative displacement maps and cumulative displacement streaming time series at 15 pre-defined points of interest.

The GPS network is based on a set of single frequency stations, which transmit phase data every 15 s to the main controlling unit.

In addition, a geotechnical monitoring network has been deployed in different stages since 2009, including 11 casings for periodic borehole inclinometer measurements, three borehole wire extensometers, eight water pressure transducers in open-pipe piezometers (below different depths, 16 to 50 m), and four DMS[TM] multi-parametric probes.

The monitoring network has been regularly reviewed and updated because of damages related to large slope displacements causing excessive deformations of inclinometer casings and open-pipe piezometers. At present, only four inclinometer casings are accessible and four piezometers are still measuring reliable piezometric levels. The four DMS[TM] columns (operated by CSG srl, Italy) collect water level and subsurface displacement data every 30 min, at measurement points in quasi-open holes and located every 1 m along columns of different lengths (12, 80, and 110 m). A weather station is located at about 2,200 m a.s.l. close to the ridge of Mont de La Saxe and acquires a complete set of data for temperature, rainfall, and snow depth data allowing for evaluation and modeling of snow melt (Broccolato et al. 2011a; Crosta et al. 2011, 2012a).

Analysis of monitoring data

Monitoring data, gathered by different types of sensors at both slope surface and depth, have been integrated and processed in order to (1) improve the understanding of the rockslide kinematics and provide a framework for further analysis, and (2) investigate the relationships among different triggers (i.e., rainfall and
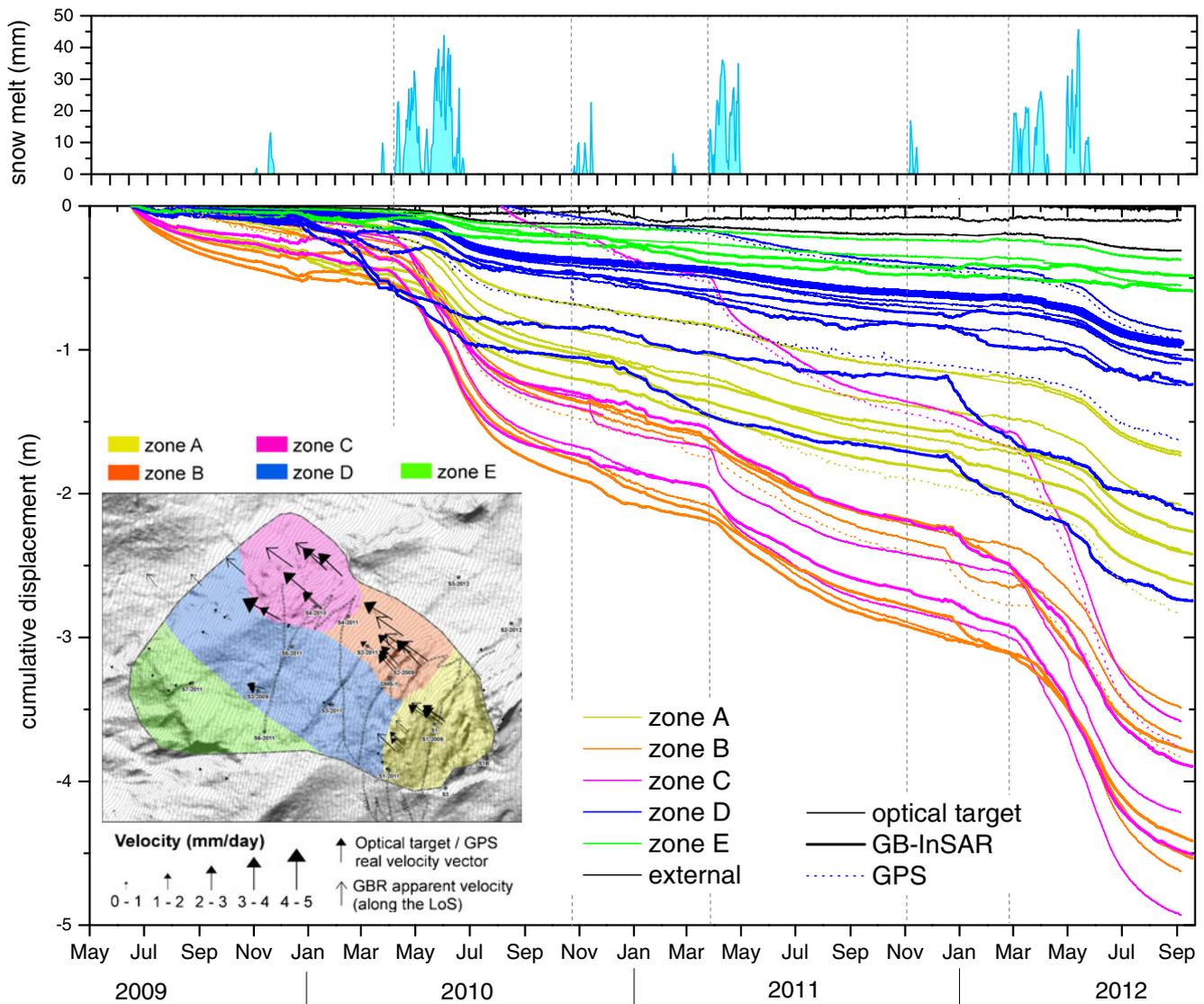
Fig. 7 Cumulative displacements measured by GB-InSAR LisaLab equipment (15 streaming points), GPS (five automatic stations), and total station (31 optical targets) (see Fig. 5 for their location). In the *inset*, the landslide is subdivided into five zones, with color code corresponding to the displacement temporal series. Average velocity vectors are also shown in the map

snowmelt) and the rockslide response. A sound knowledge of these aspects of landslide dynamics is required in order to provide reliable landslide forecasting and emergency management measures.

Figure 7 shows ground surface displacement data from June 2009 to September 21, 2012. The quality of the measurements and the redundancy of the system are demonstrated by the very close agreement between measurements obtained by means of different techniques (GPS, GB-InSAR, total station). This has also been demonstrated during some emergency phases when both GB-InSAR and total station measurements have been able to follow recent, minor failure events (May and September 2012).

The spatially distributed information obtained by GB-InSAR measurements presented in the form of geo-referenced cumulative displacement maps provides a consistent format to revise and integrate all the available investigation and monitoring data and to improve the knowledge of the kinematics and style of activity of

this complex landslide. In particular, the patterns of displacement derived from the analysis of time series extracted from the entire stack of GB-InSAR cumulative displacement maps have been evaluated against surface morphological evidence and borehole information. This allowed a subdivision of the rockslide into five zones (inset in Fig. 7).

The landslide head (zone A) shows a strong morphological irregularity, evidenced by a rapid evolution of shear fractures, opening or closing tension cracks, and intensely broken rock mass. The downhill limit of the head is formed by steep slope sectors with multiple, discontinuous rock outcrops, below which slope continues with no major scarp down to the slope toe (almost 500 m wide), which is marked by an intensely broken rocky cliff. The landslide body downslope of zone A can be subdivided into four sectors roughly parallel to the slope strike and dip direction. The NE right hand sectors (zones B and C) show higher rates of displacement, between 1 and 1.6 m/a, and are covered by abundant
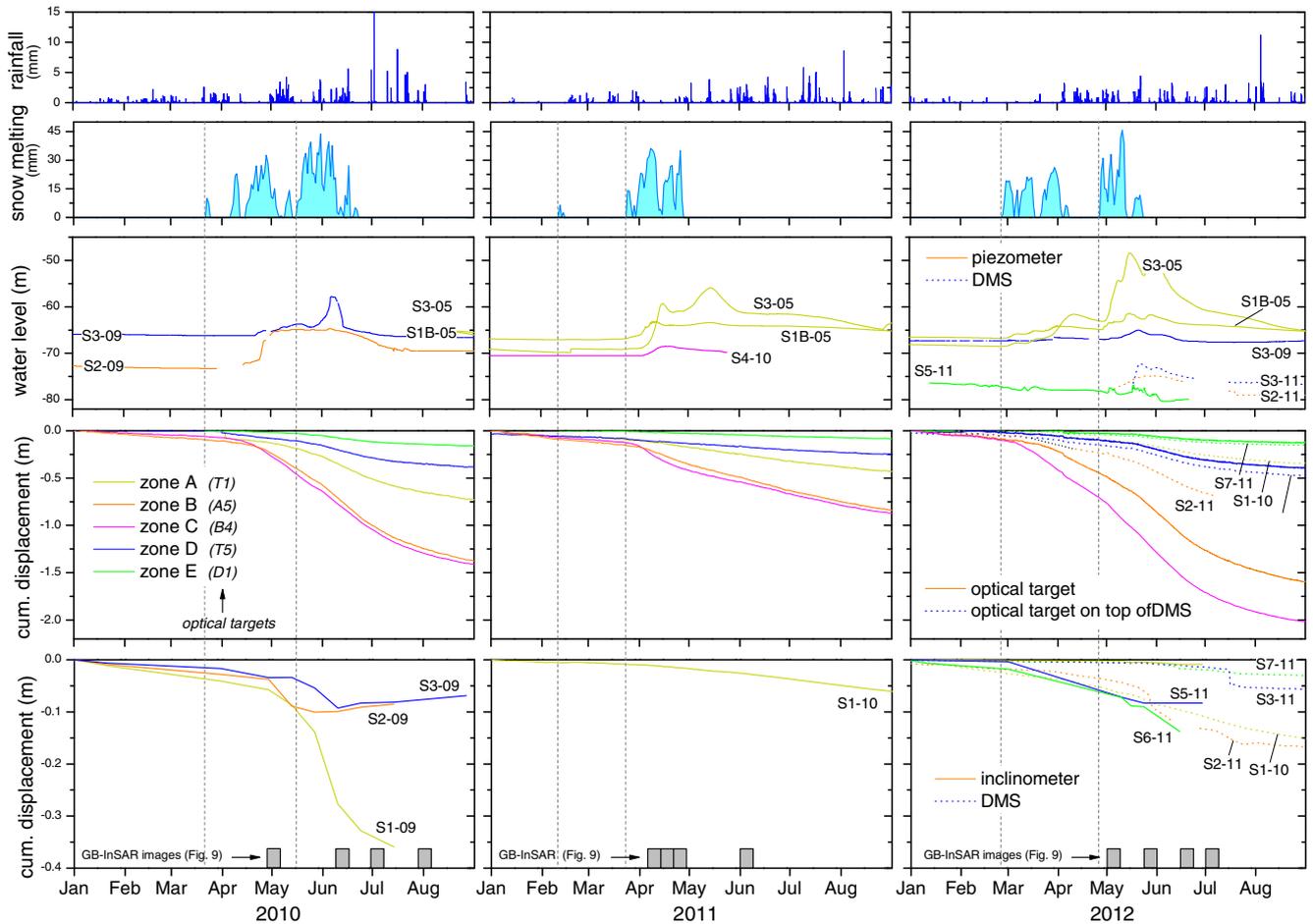
Fig. 8 Comparison between optical targets (T1, A5, B4, T5, D1), inclinometer, and DMS cumulative displacements with rainfall, snow melt, and piezometric level during the 2010–2012 season. *Hatched vertical lines* point to the beginning of each major snowmelt period. *Gray bars* indicate the intervals for the GB-InSAR maps presented in Fig. 11

loose debris with sparse vegetation. The central sector (zone D) shows a spatially variable state of activity with displacement rates ranging between 0.3 and 1 m/a. Finally, the SW or left hand sector (zone E) is well vegetated and does not show clear evidence of activity.

In general, time series of displacements available over three complete seasonal cycles (i.e., 2010, 2011, 2012) show a clear seasonal pattern with sudden acceleration stages during snow melting periods, followed by declining movement rates (usually April to June, with minor shifts between different years; Fig. 7). Less snow cover in 2011 resulted in a lower degree of activity of the landslide, especially in the head (zone A) and in the central (zone D), and western (zone E) sectors. The SW part of the landslide generally shows a significantly smaller activity with average velocity between 0.05 and 0.15 m/a. Direct rainfall during the summer period does not seem to significantly control landslide activity (Fig. 8). In contrast, available data suggest that rockslide acceleration occurs immediately after the beginning of snowmelt. Sectors located at lower altitudes (zones C and E) respond slightly before the upper sectors, presumably because of earlier snowmelt and the more abundant fine debris material typical of these areas, and/or higher local degree of saturation of the landslide mass. The NE rockslide sector (i.e., zones B and C) is always characterized by higher

displacement rates as compared to zones A, D, and E. From a temporal point of view, displacement rates measured during accelerating periods of 2010 and 2011 are similar, whereas much higher values were recorded during 2012. In this period, a sharp acceleration of zone C has been detected (i.e., displacement of about 2 m in less than 2 months for some optical targets and GPS stations), possibly indicating a significant step ahead of the rockslide system towards failure.

It is also worth noting that continuous slow slope movements are recorded during every cold-dry season. They occur at a constant rate, interposing themselves between seasonal stages of sudden acceleration/slowing phases, occurring when the groundwater level is at or just below the recognized shear zone. This possibly reflects the occurrence of an overall creeping rockslide behavior related to rock mass fatigue and damage.

Inclinometer and multi-parametric borehole probe (DMS) readings allow a comparison between surficial and deep movements and to evaluate the sensitivity of deep displacements to the rockslide triggers (rainfall and snow melting). Figure 8 supports a consistent link between the ground surface and deep response of the rockslide system to the same triggering inputs. Deep-seated displacements start slightly later (approximately 7 to 10 days) and grow faster than ground surface ones. As an example, the DMS
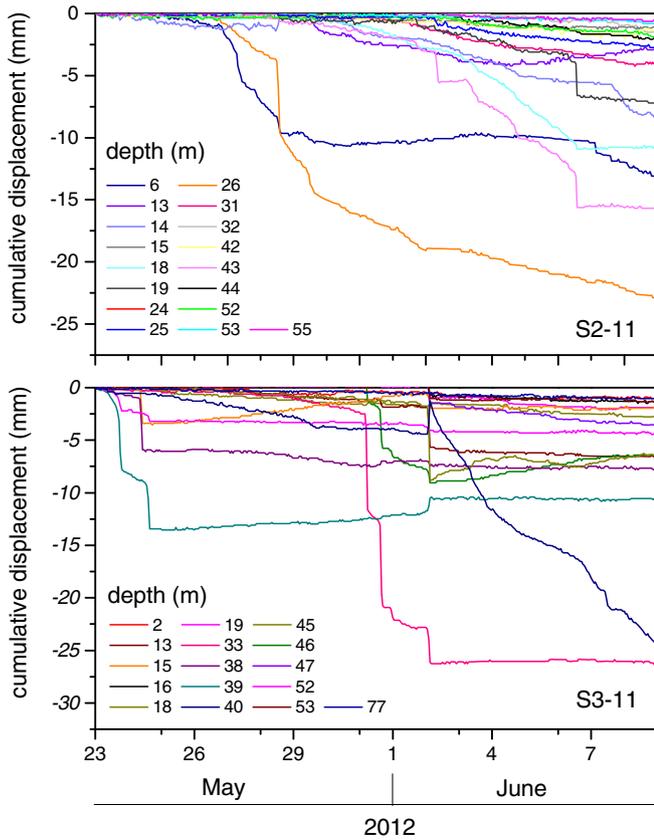
Fig. 9 DMS cumulative displacements measured at different depths within two boreholes (see Figs. 5 and 10), showing the acceleration during the 2012 spring snowmelt phase

intervals) since the beginning of the snowmelt, corresponding to the progressive increase in the water level measured by the piezometric cells. Once a threshold groundwater level is reached, a sharp, step-like acceleration takes place. Rockslide response measured by traditional inclinometric devices appears to be more linear: this probably derives from the fact that no measures have been taken in the period from March 1 to May 10, when the strongest acceleration was expected, and displacements are spread over the 15-day measurement interval.

A similar behavior, but on a shorter time scale, has been observed in DMS data and two examples are shown in Fig. 9. This shows the short-term reaction of the rockslide at different depths to snowmelt during the 2012 late spring. The DMS data describe a sort of stick slip behavior with successive steps characterized by a progressively accelerating displacement up to an almost instantaneous movement followed by a subsequent step. This behavior is evident along the main localized shear zone (see Figs. 9 and 10) and could be either related to stick-slip behavior or to rapid changes in water pressure along the shear zone.

Piezometric levels in open stand pipes have been monitored on an almost continuous basis (see Fig. 8), and changes up to about 10 m have been observed in a relatively short time and associated to major snowmelt periods. No clear or relevant variations have been observed following major rainfall periods. Discontinuity in measurements is due to the large annual displacements at the failure surface, which cause rapid deterioration or complete cutting of the piezometers, and damage of the pressure transducers. Piezometric level at the S1-09 borehole within the rockslide head is generally measured 40 m below the active failure surface and at the base of a 90-m-thick broken rock mass sector.

Spatial–temporal evolution of the movement

The analysis of GB-InSAR datasets reveals relationships between the temporal and spatial styles of activity of different rockslide

column installed in borehole S3-11 (Fig. 8) shows a slow displacement rate in the downhill direction (measured at 1-m depth
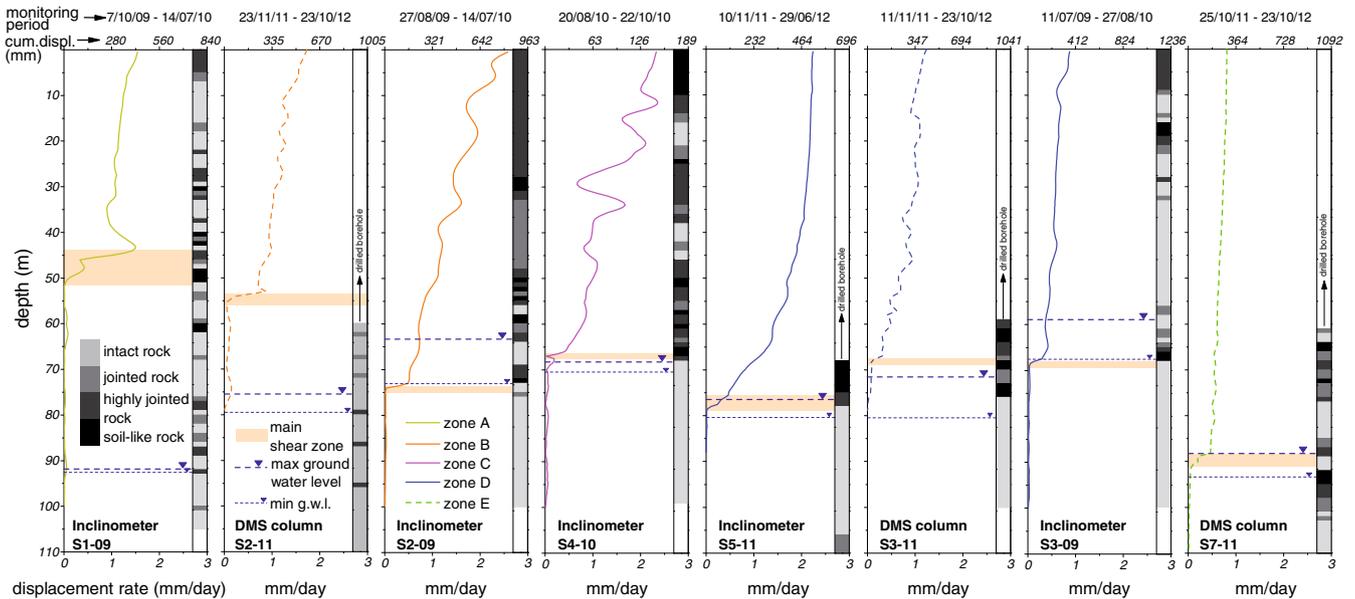
Fig. 10 Inclinometer and DMS cumulative displacement plots and average displacement rate at different rockslide sectors (A to E; see Fig. 5 for position) for different total measuring intervals (see dates above each plot) compared with simplified fracture density logs. Percussion drilling intervals, main shear zone extent, and groundwater table levels are shown

zones to be assessed in response to the triggering inputs. In particular, cumulative displacement maps have been processed in order to obtain maps of the incremental displacements for 7-day time intervals (Fig. 11). These maps show the seasonal trends and sudden changes (i.e., accelerating events) of displacements in parts of the landslide characterized by different behaviors (i.e., zones A to E). This analysis allowed us to identify the following clear rockslide "spatial activation sequence":

1. initial (precursory?) displacements start within the scree deposit at the landslide toe before activating the main rock slide area, manifested by small rockfall events detaching from the main rockslide body;
2. initial rockslide accelerations take place during the first part of the snowmelt period in the NE, faster rockslide sector (zones B and C, characterized by the sharpest morphological evidence);
3. at the end of the snowmelt period, also corresponding to the highest groundwater table stages, the entire rockslide body becomes involved in a generalized movement (displacements extending to zones A and D), with an inferred failure surface day-lighting either at the base of the landslide rocky toe or at the apex of the scree deposit;

4. during the recession stage of groundwater table, the activity again becomes confined to zones B and C, progressively slowing until the end of the activation period. The length of the groundwater recession stage varies from year to year, due to the possible contribution of snow depth, temperature pattern, and rainfall periods following the snowmelt.

2D groundwater flow model

Groundwater flow modeling allows to verify both the consequences and the validity of some of the surveyed characteristics, and of the assumptions made about the role played by major features (e.g., morphostructures) and local to regional topography (Gleeson and Manning 2008). At the same time, groundwater modeling offers the means for assessing the oscillation of groundwater level which is a major input in rock slide and deep-seated gravitational slope deformation modeling (Crosta and Agliardi 2003; Guglielmi et al. 2005; Pisani et al. 2010).

To this aim, both 2D and 3D groundwater flow modeling of the slope have been performed (Crosta et al. 2011). To better outline the general behavior of the slope, the results of a 2D saturated–
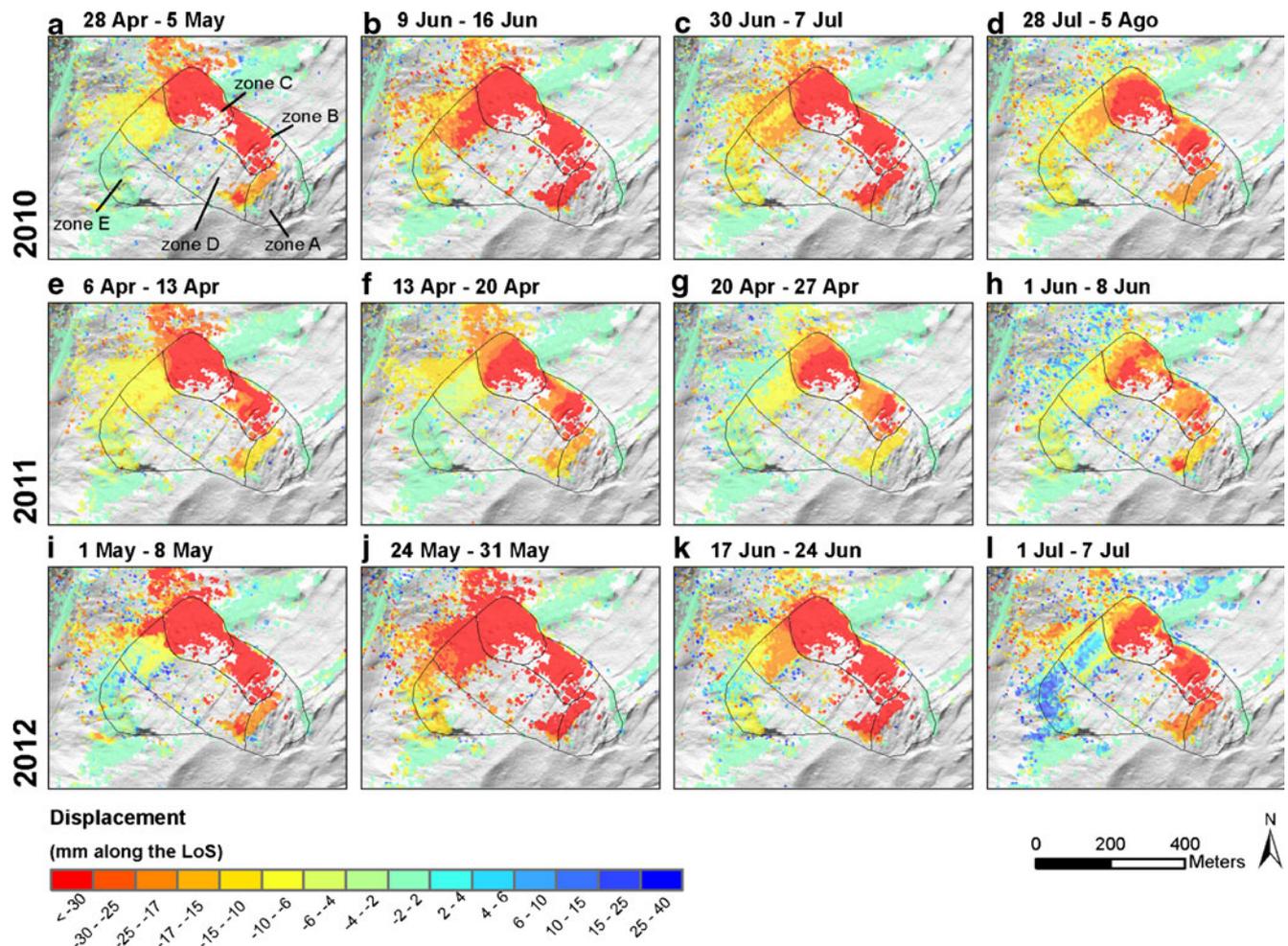
Fig. 11 GB-InSAR maps of incremental displacement at 7-day intervals through the main snow melting periods in 2010, 2011, and 2012. The same color legend has been applied through the figures to show the progressive seasonal acceleration and deceleration of the different rockslide sectors (A to E zone limits are traced in *black*)

unsaturated flow model are presented. The model considers the presence of a detensioned upper rock slide mass and a slightly detensioned deep-seated gravitational instability (see schematic cross-section in Fig. 3). The two instabilities are bounded at their base by thin cataclastic shear bands. The hydraulic conductivity values have been estimated by borehole observations and measurements, infiltration testing, geophysical investigation data, and laboratory tests on samples of cataclastic breccia. Water characteristic curves have been assumed tri-linear with parameters typical of coarse (e.g., sandy–silty soils for broken weathered rock mass) up to very fine soils (e.g., cataclastic shear bands). Seismic velocities allowed us to estimate a porosity value for each of the main contour intervals in Fig. 4. In particular, some empirical relationships linking compressional wave velocity (V_p) with porosity (n) (Wyllie et al. 1956, 1958; Watkins et al. 1972; Lama and Vutukuri 1978; Kirsch 2006), and with degree of jointing (Sjögren et al. 1979) have been presented in the literature. Following, for example, Watkins et al. (1972) and Kirsch (2006), a progressive decrease in porosity with depth can be associated to the wave velocities presented in Fig. 4 (V_p=1,350 m s^{-1}, n=0.30; V_p=1,750 m s^{-1}, n=0.25; V_p=2,450 m s^{-1}, n=0.19; V_p=3,000 m s^{-1}, n=0.16). A similar trend can be derived for RQD values or linear (1D) joint frequency (Palmstrom 1995). The change in elastic wave velocity with RQD and 1D joint frequency allowed us to attribute fracture intensities to slope sectors delimited through seismic refraction tomography.

Grain size analyses and laboratory permeability tests provided a range of hydraulic conductivity values for the breccia level ranging between 10^{-7} and 10^{-9} m s^{-1}. These values are in good agreement with measurements on cataclastic breccias at the base of large deep-seated deformations (Crosta et al. 2012a, b) and from cataclastic materials described in the literature (Fischer et al. 1998; Burgi et al. 2001; Riedmüller et al. 2001; Sausgruber and Brandner 2003; Mansour et al. 2011).

The stage of development of the rockslide and the amount of cumulative displacements play a major role in controlling the breccia parameters. In fact, it is reasonable to suppose that for small initial displacements the breccia will represent a level more permeable than the contiguous rock mass, especially in case of quasi-translational mechanisms. On the contrary, for larger displacements the rock slide mass will progressively break and strain localization will occur with a progressive grain size reduction by clast fragmentation and shearing. This induces a decrease in hydraulic conductivity along the basal failure zone and an increase within the fractured rock-slide mass.

On the basis of all these data and from similar studies in the literature (Agliardi et al. 2001; Binet et al. 2007; Boadu 1997; Cappa et al. 2004; Guglielmi et al. 2005; Pisani et al. 2010; Crosta et al. 2011; 2012a, b) for large rock slides and deep-seated gravitational slope deformations, it has been decided to attribute a range of values to each of the main sectors within the Mont de La Saxe slope (Fig. 12a) based on the conceptual model illustrated in Fig. 3.

The finite-elements mesh consists of 33,537 elements with an average area of about 100 m², down to about 5 m² within the cataclastic zones (Fig. 12a).

Recharge has been applied at the ground surface accordingly to the total equivalent precipitation, taking into account for snow melting in spring and early summer, evapotranspiration, and concentrated infiltration at some trenches considered continuous

and highly permeable as found from infiltration tests and borehole drilling (S1–12). The transient model was implemented by using daily time steps from July 1, 2009 to September 12, 2012, starting from head distribution simulated with a steady-state simulation. The net recharge rate has been calibrated starting from field surveys and the measurements mentioned above.

Model results show the presence of a main groundwater table, which is located at the bottom of the rockslide. Different values of hydraulic conductivity relative to the different materials result in different groundwater geometries, with perched groundwater table above a deeper unsaturated zone, but these models were less successful in the calibration process, and a full description of the possible results is out of the scope of this paper. This groundwater table varies during the hydrologic year between 5 and 10 m, with maximum levels in late spring (Fig. 12c) and minimum values in early spring, before snowmelt occurrence (Fig. 12d). The hydrological dynamics in proximity of the rockslide shear zone is complex. Above the shear zone, the hydrologic response following snowmelt is extremely rapid (Fig. 12b), as observed in monitored boreholes (see Fig. 8). This response seems mainly controlled by melting within the rockslide area or convoyed to the rockslide by high permeable materials (e.g., trenches). Below the shear zone, the response is significantly slower (Fig. 12b), and it is associated with a deep circulation system which is also supported by the higher mineralization observed at the springs located at lower elevation. These results support the idea that the groundwater recharge close to the rockslide is mainly to be attributed to a major vertical infiltration and redirection by highly permeable structures (e.g., trenches, counterscarps).

A simplified approach for the modeling of the rockslide temporal evolution

The La Saxe rockslide movement (Figs. 7, 8, and 9) is here interpreted as the result of two specific mechanisms:

(a) a sort of "creep"-driven movement that is always present even under dry-winter conditions, when the water table is either below or close to the failure surface, and
(b) a superimposed (seasonal) acceleration-slowing trend directly related to the snow melt (late spring–early summer) and to the consequent water table fluctuations, which disappears when the water inputs are reduced (late summer and winter conditions).

In order to model this type of rockslide behavior, a correct approach should satisfy the following monitoring-driven guidelines:

– modeling of the material time-dependent mechanical behavior by means of a viscos-plastic constitutive law capable of capturing creep phenomena (di Prisco and Imposimato 1996; di Prisco and Zambelli 2003);
– assuming the water table fluctuation as the main input to reproduce the late spring–early summer acceleration;
– considering the 3D behavior while maintaining simplicity to allow the implementation within the EWS for risk mitigation.

As it was illustrated in the previous sections, the Mont de la Saxe rockslide is a complex landslide, in which the displacement field is in general a function of space and time. The rockslide displacements have thus to be expressed as a vector function $u(x, y, z, t)$ and, at any instant of time, this vector function should be suitably
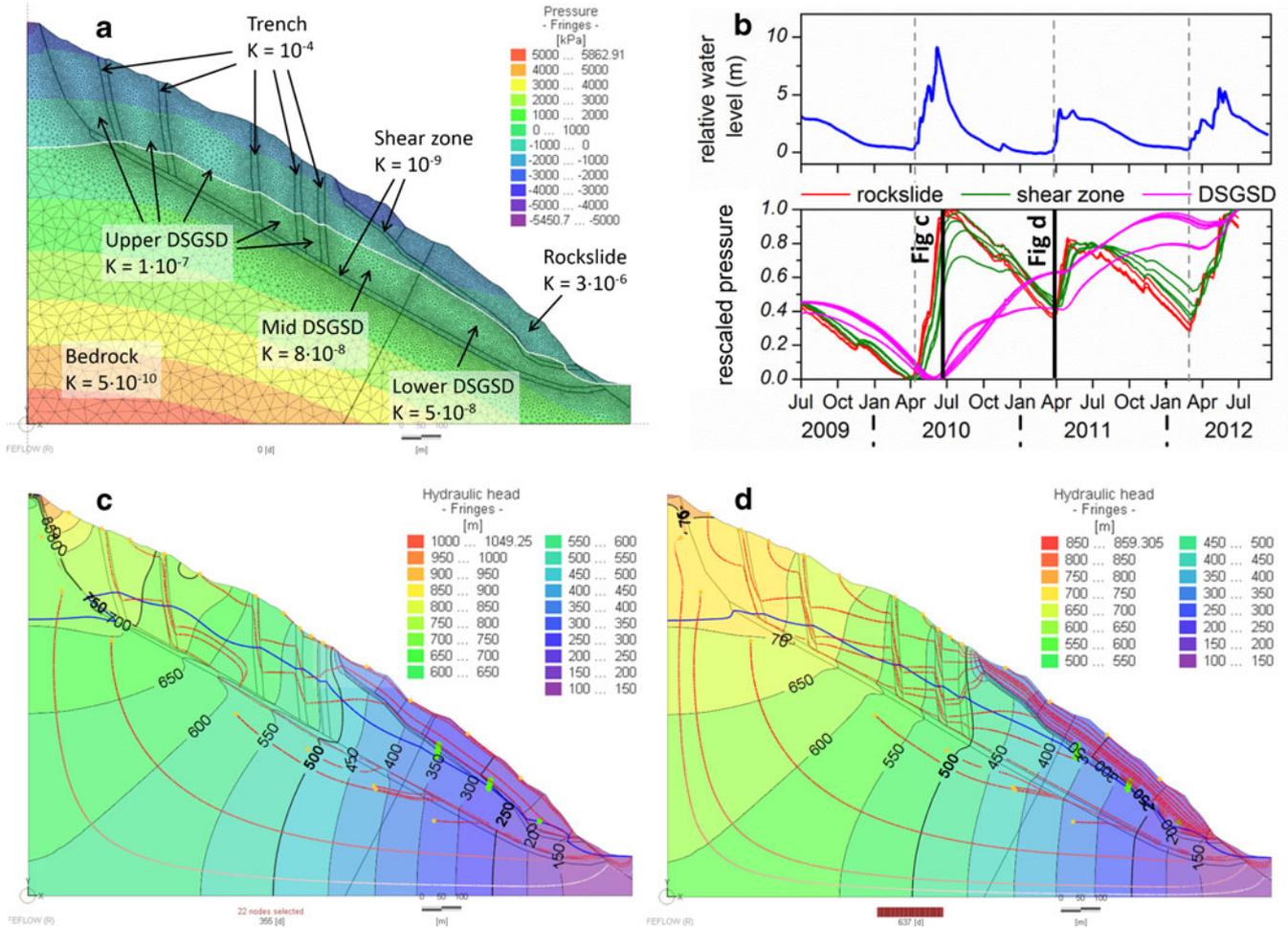
Fig. 12 2D transient groundwater model of the slope. **a** Model setup and results of the steady-state simulation used as initial condition for the transient model; **b** comparison of relative water table averaged from monitored data (cf. Fig. 17a) and pressure variations for observation points within the model; **c** transient model results corresponding to maximum water table level (June 20, 2010); transient model results corresponding to minimum water table level (April 29, 2011). The reported values for the hydraulic conductivity are the calibrated values for this model, and slight changes in values can generate the formation of perched groundwater tables. Formation of a surficial and a deep groundwater flow path is shown in the model, together with the role of more permeable trench material and less permeable cataclastic shear bands

evaluated from monitoring data. Nevertheless, in the following, for the sake of simplicity:

(a) the entire landslide mass will be subdivided into a finite number n of rigid blocks, where both the direction and the intensity of the displacement vector are assumed constant within each volume. This implies that the dispersion velocity both in direction and in modulus within each volume is neglected;

(b) within each volume the direction of the displacement vector is assumed to be constant, that is:

$$u' = x(t)u''$$ ([1])

where $x(t)$ is a scalar function describing the temporal evolution of the displacement in each volume, whereas u'' is the unit vector describing the direction of displacements.

In this study, Newmark's approach (1965) and Perzyna's theory (1963) have been coupled (Frigerio 2010; Secondi et al. 2013) to model the rockslide behavior. According to Newmark's approach,

each volume in which the rockslide is subdivided is interpreted as a rigid block (Fig. 13), where the active forces taken into account are (1) the weight, (2) the inertial forces, and (3) the seepage force deriving from the water table level which is a function of time, $\Delta h_w(t)$. All the non-linearities are lumped both (1) at the interface between the rigid block and the bedrock and (2) at the interface between each volume and those surrounding it. The mechanical response of these interfaces is assumed to be rigid-visco-plastic. Similar approaches have been introduced in the recent past by Karampatakis and Hatzigogos (1999), and Puzrin and Schmid (2012).

In the following sections, (1) the model and the methodological approach adopted to simplify the relatively complex 3D geometry of the rockslide, (2) the capability of this approach to reproduce the displacement history of La Saxe rockslide, and (3) its possible use in EWS will be discussed.

The 1D model

According to standard visco-plasticity, the plastic flow rule is modified, the consistency condition removed, and the visco-
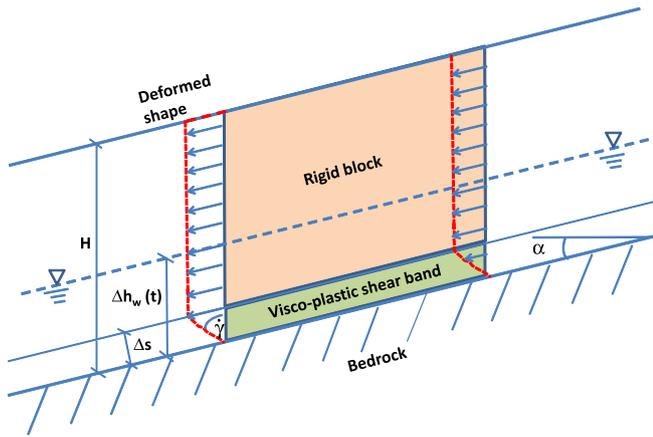
Fig. 13 Proposed mono-dimensional block model with main geometrical elements (shear band thickness, elevation of the water table, depth of failure zone, slope inclination)

Fig. 14 Rate of axial deformation as a function of the parameter of viscosity

plastic strain rate tensor $\dot{\varepsilon}_{ij}^{vp}$ in soil mechanics is defined as follows:

$$\dot{\varepsilon}_{ij}^{vp} = \widetilde{\gamma} \; \Phi(f)\frac{\partial g}{\partial \sigma'_{ij}} \qquad ([2])$$

where f is the yield function, g the plastic potential, $\widetilde{\gamma}$ a positive constitutive parameter, σ_{ij} the effective stress tensor, and $\Phi(f)$ the viscous nucleus. Owing to the simplicity of the geometry taken into consideration, and under the assumption that the material within the process zone has reached a sort of critical state, that is volumetric strain rates are nil, Eq. [2] becomes

$$\dot{\gamma}^{vp} = \widetilde{\gamma} \; \Phi(f) \qquad ([3])$$

where the left term is the visco-plastic shear strain rate developing within the shear band while $\widetilde{\gamma}$ is a viscous constitutive parameter (calibrated either on experimental data or by means of back analyses). Since it has been assumed that: (1) strain rates are negligible within the sliding mass not belonging to the shear band, (2) shear strain rates, located within the shear band of thickness Δs positioned at the interface, are constant within the shear zone, and (3) elastic-strain rates are negligible, the sliding mass displacement rate $\dot{x}$ can be simply related to $\dot{\gamma}$:

$$\dot{x} = \Delta s \, \dot{\gamma} = \Delta s \, \dot{\gamma}^{vp} = \widetilde{\gamma} \; \Delta s \; \Phi(f) \qquad ([4])$$

Here in the following, a simple bi-linear formulation for the viscous nucleus (Fig. 14) has been chosen:

$$\Phi(f) = \langle f \rangle \qquad ([5])$$

where brackets imply the viscous nucleus to coincide with the yield function for $f > 0$ and nil for negative values of f. In the model here employed, the f function is written in an explicit non-dimensional form as follows:

$$f = \frac{\tau - \tau_{res}}{\sigma'_n} \qquad ([6])$$

where τ represents the effective shear stress and τ_{res} the yield threshold, depending on the adopted failure criterion, whereas σ_n' represents the average effective normal stress at the sliding plane depth.

In each block, the effective shear stress can be interpreted as the sum of both the static term, τ_{stat} (i.e., weight of the masses acting on the system), and a dynamic term, depending on both the acceleration along the x-direction $\ddot{x}$ and the landslide mass over the landslide contact area $m^{\star}$:

$$\tau = \tau_{stat} - m^{\star} \ddot{x} \qquad ([7])$$

The static term is in general evaluated as:

$$\tau_{stat} = \left(W'[\Delta h(t)]\sin(\alpha) + J + F^{rel} \right) \big/ A \qquad ([8])$$

where A stands for the total contact area, W' is the buoyant weight (above the water table is assumed in dry conditions, whereas below the buoyany material weight is used), J is the total seepage force, $\Delta h(t)$ the groundwater table level varying with time t, whereas term F^{rel} stands for the resultant of both the forces transmitted by the lateral boundaries of each block and the forces transmitted by the uphill blocks to the downhill ones. In case the number of blocks is equal to one, F^{rel} nullifies. For the sake of simplicity, a Mohr–Coulomb failure criterion has been chosen

$$\tau_{res} = c' + \sigma'_n \tan\phi'_{res} \qquad ([9])$$

where σ_n' stands for the effective force normal to the sliding plane N' over the total contact area.

The strategy employed to calculate, in an uncoupled way and for each block, both F^{rel} and σ_n', in case $n>1$, will be clarified in the following section.

In case f is positive, by substituting Eqs. [4], [6], and [7] into Eq. [5], and by introducing the geometrical and constitutive parameters, we obtain for each block an equation of the following type:

$$a \ddot{x} + b \dot{x} + c = 0 \qquad ([10])$$

where coefficients a, b, and c depend on time and can be derived from the previous equations. In case $f<0$, coefficients a, b, and c change and in particular term b nullifies since visco-plastic displacements disappear. In both cases, the slope displacements can

be numerically calculated by employing a standard finite difference integration scheme.

Spatial discretization

The spatial discretization of the rockslide and the groundwater table oscillation $\Delta h_{wi}(t)$ (with $1 < i < n$) are evaluated by means of an ad hoc averaging procedure (Figs. 15 and 16).

The first attempt consisted of assuming one single block ($n=1$, ABCDE). The lateral forces T_{Li} (Fig. 15), due to the friction between the lateral faces of the block and the rock boundary, are considered as in Eq. [11]. In this case, the average water table fluctuation obtained by means of a 3D reconstruction of the winter and summer groundwater table surface (discretization #1 in Fig. 15 and Table 1) is always below the average elevation of the failure surface. Therefore, given that discretization #1 is too poor, the model simulation is not affected by the groundwater table oscillation.

Discretization #2 (Fig. 15) considers four blocks (A, BC, D, E), discretization #3 (Fig. 15) considers the same five blocks/zones (A, B; C, D, E) of Fig. 7. Each zone is supposed to correspond to a block of specific inclination, height, width length, and shear band thickness as is shown in Table 1. The interaction between the blocks has been taken into account by assuming lateral and normal forces (Fig. 15). Normal forces N_{Ai} are related to the active pressure exerted by the uphill blocks on downhill blocks while normal forces N_{oi} are due to the mutual interaction between blocks moving at the same speed. These forces have been evaluated by assuming:

$$T_{Li} = 1/2\gamma H^2{}_i L_i k_0 \tan\phi$$
$$N_{oi} = 1/2\,\gamma\,H^2{}_i B_i k_0 \qquad\qquad ([11])$$
$$N_{Ai} = 1/2\,\gamma\,H^2{}_i B_i k_a$$

where k_o and k_a represent the at rest and the active pressure coefficients, respectively. In discretization #3 (Fig. 15), the interaction force between block B and C has been evaluated by

employing the at rest pressure coefficient since the monitored displacements are very similar, while for block B, C, and A the active pressure coefficient was employed since block BC is moving faster than A.

Once the rockslide mass is split into subzones, the same subdivision can be applied to the groundwater table surface (Fig. 16). For each zone (i), the minimum, $h_{wi}{}^{MIN}$, and the maximum, $h_{wi}{}^{MAX}$, groundwater table positions are evaluated (see Table 1) after a 3D reconstruction of the minimum (winter) and maximum (summer) water table level as is shown in Fig. 16. In contrast, function $\Delta h_{wi}(t)$ is assumed to be unique for all the i-blocks.

Numerical simulations

The model has been applied and validated by considering the 2010–2012 displacements of Mont de La Saxe slope. Calibration, by back analysis, of the model parameters (viscous parameter, $\widetilde{\gamma}$, and strength parameters, c' and ϕ_{res}') has been carried out by using the already described displacements and groundwater datasets. In contrast, the shear band thickness Δs_i is assumed to be constant in the landslide area and it has been derived from inclinometer measurements.

The analyses have been performed systematically by considering discretization #1, #2, and #3.

In all the cases taken into account, for each "homogenized" zone (i), the following procedure was followed:

- evaluation of function $x_i(t)$ by an averaging procedure of the measured cumulative displacements (e.g., Fig. 7);
- estimation of the input function $h_{wi}(t)=h_{wi}{}^{MIN}+\Delta h_{wi}(t)$; where $h_{wi}{}^{MIN}$ (Table 1) is evaluated from a 3D reconstruction of the lower groundwater surface (Fig. 16a) while $\Delta h_{wi}(t)$ (Fig. 17a) is obtained by means of an averaging procedure of the piezometric measurements and is assumed constant for all the zones. If a more continuous set of piezometric data were available at different points within the rockslide, the most convenient
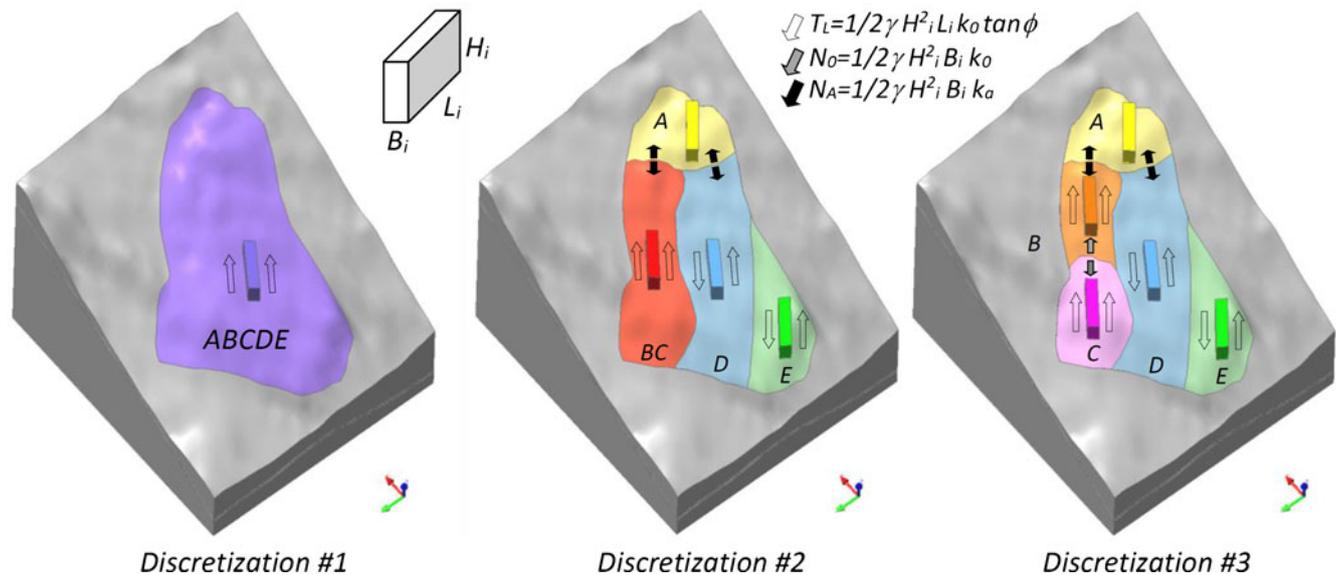
Fig. 15 Different discretization adopted in the model: #1 single equivalent rockslide block; #2, #3 multiple equivalent rockslide blocks, one for each representative rockslide sector
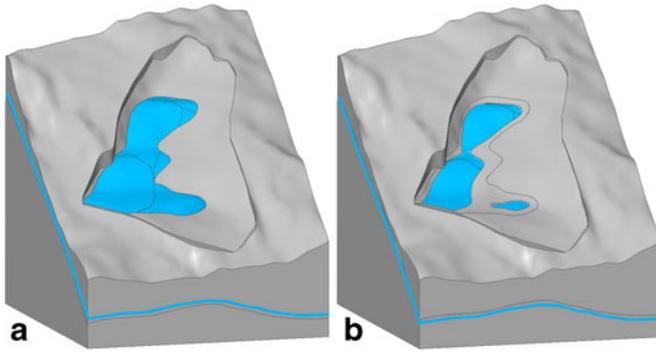
Fig. 16 3D view of the summer (or *high*) (**a**) and winter (or *low*) (**b**) groundwater table surface. *Colored polygons* refer to the above five sectors' rockslide zoning

approach would consider a function $\Delta h_{wi}(t)$ different for each zone;

- definition of the geometrical input parameters (inclination α_i, height H_i, width B_i, length L_i of the block, and shear band thickness, Δs_i); α_i, H_i, B_i, and L_i are easily evaluated from a geometrical 3D averaging of zone (i) using GIS tools, the shear band Δs_i is evaluated by averaging borehole and inclinometric observations. Following this procedure, and considering the vertical distribution of measurements as well as the stratigraphic borehole log, the shear band thickness has been set equal to 1 m. The values for the mean shear band and damage zone thickness agree also with results from empirically derived relationships (e.g., Faulkner et al. 2010);

- model calibration to set the viscous and strength parameters. The viscous parameter, $\widetilde{\gamma}$, has been evaluated by back analysis for discretization #1 (Fig. 15) and then maintained in all successive simulations (discretization #2 and #3 in Fig. 15). The strength parameters (c' and ϕ_{res}') are the output of each back analysis; concerning the large magnitude of displacements, a nil value of cohesion has been assumed;
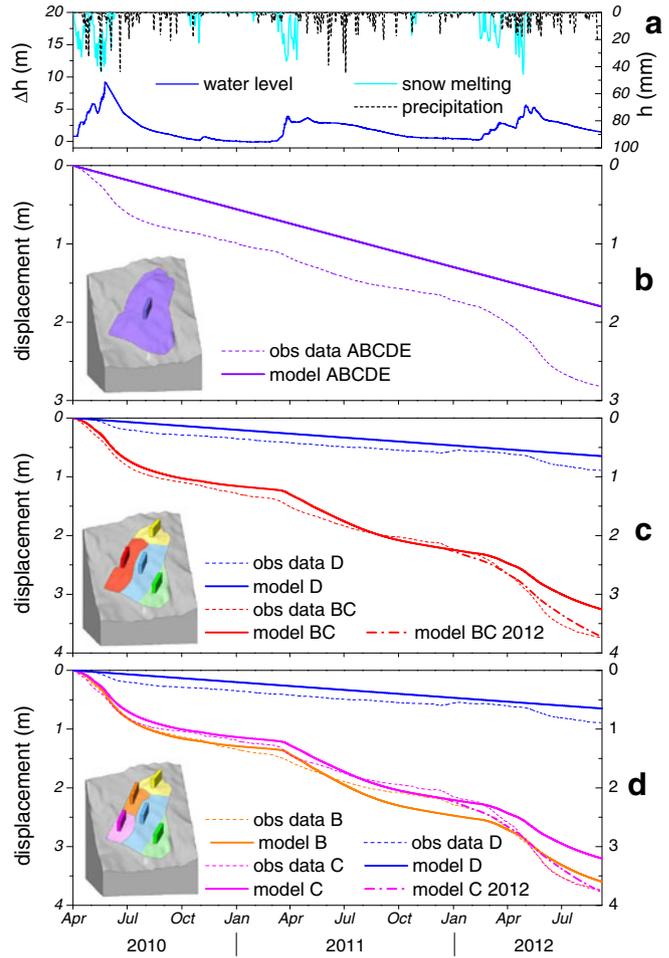
Fig. 17 Plots comparing the results of the visco-plastic model to the measured cumulative displacements for different discretization schemes (1 to 3) of the rockslide mass and of the piezometric surface. Color codes refer to the different subareas. Model 2012 shows the results of a best-fitting model for the 2012 displacements only (see also Table 2)

Table 1 Geometric parameters for each rockslide sector relative to each of the three discretization schemes (Fig. 15)

Discretization	Zone	Slope inclination α (°)	Depth failure surface H_i (m)	Transversal length B_i (m)	Longitudinal length L_i (m)	Shear band thickness Δs (m)	Depth h_w^{MIN} (m)	Depth h_w^{MAX} (m)
1	ABCDE	33.5	62.4	280.0	620.4	1.00	77.7	68.5
2	A	39.0	60.8	180.0	169.2	1.00	86.5	77.3
	BC	33.1	74.1	114.7	427.3	1.00	63.4	54.2
	D	36.8	59.5	140.0	443.3	1.00	74.5	65.3
	E	25.8	43.3	115.0	279.7	1.00	100.5	91.3
3	A	39.0	60.8	180.0	169.2	1.00	86.5	77.3
	B	37.2	78.0	107.5	198.9	1.00	64.5	55.3
	C	29.0	70.3	122.0	226.6	1.00	62.3	53.1
	D	36.8	59.5	140.0	443.3	1.00	74.5	65.3
	E	25.8	43.3	115.0	279.7	1.00	100.5	91.3

Averaged values have been obtained from GIS calculations on interpolated surfaces (piezometric and failure plane)

Table 2 Values for the mechanical parameters adopted in the 1D visco plastic model to compute displacements for each one of the discretization schemes presented in Fig. 15

Discretization	Zone	c' (kPa)	ϕ' (°)	γ (1/s)
1	ABCDE	0.00	30.65	4.00E−06
2	BC	0.00	27.90	4.00E−06
	D	0.00	36.98	4.00E−06
2* (degradated)	BC (2012)	0.00	27.70	4.00E−06
3	B	0.00	29.04	4.00E−06
	C	0.00	26.69	4.00E−06
	D	0.00	36.98	4.00E−06
3* (degradated)	C (2012)	0.00	26.46	4.00E−06

From the analysis of the obtained results, we can derive the following remarks:

- It is evident that in case of discretization #1 (Fig. 17b) the model does not reproduce the seasonal oscillation related to snowmelt, rainfall, and water table oscillation (Fig. 17a). In fact, the averaged groundwater table level is always below the averaged shear band depth. Nevertheless, this simulation is very useful (1) to evaluate the viscosity-driven movements, (2) to assess the viscous parameter, γ, and (3) to constrain the strength parameters (Table 2) representative of the average rockslide behavior.
- Discretization #2 (Fig. 17c) for zones B, C, and D reveals the capability of the model to describe the displacement oscillation due to groundwater table changes. This also suggests the necessity of considering a subdivision into different zones. In fact, by properly considering the input parameters for each zone, the different behavior of zone D (with a maximum groundwater table below the shear band) with respect to zone BC is quite well captured, although the same value for the viscous parameter is employed. The discrepancy in the last year between data and predictions suggests the occurrence of a degradation process that seems to be suitably described by a slight reduction in the friction angle (see Fig. 17c, model BC 2012).
- the finer discretization #3 (Fig. 17d) shows results similar to discretization #2.

Conclusions

Large rockslides can pose significant hazards, and the understanding of their mechanism and stabilization requires acquisition of comprehensive data sets. The case study of the Mont de La Saxe rockslide was presented together with the monitoring dataset to show the relevance of surface and subsurface measurements for a better understanding of the rockslide behavior. A continuous set of GB-InSAR measurements has been acquired and time histories extracted for about 120 points, forming a network of virtual sensors. These provide a robust description of the ground surface displacement field for most of the rockslide. Subsurface displacements are available to constrain failure surface geometry and time of reaction to external perturbations.

The monitoring dataset allows the subdivision of the landslide into zones with different behavior and sensitivity to triggering, which are also associated with different failure scenarios (e.g., size, expected runout). Each zone can be provisionally considered as an independent block or as a block interacting in different ways with neighboring blocks, and for which stability and dynamics can be modeled. To this aim, a visco-plastic one-dimensional dynamic model is presented and applied. The model has been calibrated and applied to the available displacement data showing a good performance at predicting rockslide displacements during acceleration and deceleration phases controlled by groundwater level oscillations. It is important to stress that all the simulations have been carried out with the same viscous parameter obtained through a very basic 1D model averaging the characteristics of the entire slide. The relevance of snowmelt infiltration, ground water recharge, and increasing piezometric level has been described and discussed by performing in situ measurements, tracer testing, and some 2D groundwater flow simulations. The study of groundwater flow and the application to the prediction of the rockslide dynamics could be useful to simulate expected displacements and their accelerations due to seasonal changes and future climate changes (i.e., considering different snowmelt and rainfall distribution). The same model could be applied to verify the change in expected displacements when an efficient drainage system is put in place. Due to the extreme simplicity of the model, a real-time calibration and prediction process can be implemented in order to continuously refine the values of the model parameters. This step could be implemented in the La Saxe rockslide EWS via collection of a consistent and comprehensive dataset. In conclusion, this simple model applied by a proper zonation of the rockslide mass copes satisfactorily with the complex rockslide activity. The model seems therefore suitable for a consistent and reliable prediction of displacements directly related to hydrogeological and climate forcing. At the same time, the model is presently unable to predict a possible sudden collapse of the entire mass or of one of the sub-blocks, and this is part of the ongoing research effort by the authors. Consequently, the displacement-rate threshold values, adopted in the EWS for the case of a rapid collapse scenario, are based on previous experience on similar alpine rockslides and on the observed reaction of the rockslide. Contemporaneous overpassing of these threshold values at multiple measuring points, both at the surface and at depth, is a requirement to initiate any civil protection action and allows either to avoid false alarm or to differentiate among

the various possible scenarios (i.e., rock falls or slides of limited volume).

References

Agliardi F, Crosta G, Zanchi A (2001) Structural constraints on deep-seated slope deformation kinematics. Eng Geol 59(1):83–102

Agliardi F, Crosta GB, Frattini P (2012) Slow rock slope deformation. In: Clague JJ, Stead D (eds) Landslides: types, mechanisms and modeling, Cambridge University Press, pp 207–221

Angeli MG, Gasparetto P, Menotti RM, Pasuto A, Silvano S (1996) A visco-plastic model for slope analysis applied to a mudslide in Cortina d'Ampezzo, Italy. Q J Eng Geol 29:233–240

Antoine P et al (1979) Geological map of France, scale 1/50,000, sheet Mont-Blanc (704). Bur. de Rech. Geol. et Min, Orléans, France

Antoine P, Pairis JL, Pairis B (1975) Quelques observations nouvelles sur la structure de la couverture sédimentaire interne du massif du Mont-Blanc, entre col Ferret (frontière italo-suisse) et la Tête des Fours (Savoie, France). Géol Alpine 51:5–23

Binet S, Mudry J, Scavia C, Campus S, Bertrand C, Guglielmi Y (2007) In situ character-ization of flows in a fractured unstable slope. Geomorphology 86:193–203

Boadu FK (1997) Fractured rock mass characterization parameters and seismic properties: analytical studies. J Appl Geophys 36:1–19

Broccolato M, Cancelli P, Castellanza R, Crosta GB, Frattini P, Tamburini A (2011a) Applicazione di modellazioni numeriche alla frana di Mont de la Saxe (Courmayeur—AO) XXIV Convegno Nazionale di Geotecnica, "Innovazione Tecnologica nell'ingegneria Geotecnica". Napoli 2:617–624

Broccolato, M., Cancelli, P., Crosta, G.B., Tamburini A., Alberto W. (2011b) Tecniche di rilievo e monitoraggio della frana di Mont de la Saxe (Courmayeur—AO). XXIV Convegno Nazionale di Geotecnica, "Innovazione Tecnologica nell'ingegneria Geotecnica", Napoli

Burgi C, Parriaux A, Franciosi G (2001) Geological characterization of weak cataclastic fault rocks with regards to the assessment of their geomechanical properties. Quart J Eng Geol Hydrogeol 34:225–232

Butterfield R (2000) A dynamic model of shallow slope motion driven by fluctuating groundwater levels. Proc. 8th Int. Symposium on Landslides. Thomas Telford, London, 1, 203–208

Cappa F, Guglielmi Y, Soukatchoff VM, Mudry J, Bertrand C, Charmoille A (2004) Hydromechanical modeling of a large moving rock slope inferred from slope levelling coupled to spring long-term hydrochemical monitoring: example of the La Clapière landslide (Southern Alps, France). J Hydrol 291:67–90

Casagli N, Catani F, Del Ventisette C, Luzi G (2010) Monitoring, prediction, and early warning using ground-based radar interferometry. Landslides 7(3):291–301

Chigira M (2005) September 2005 rain-induced catastrophic rockslides on slopes affected by deep-seated gravitational deformations, Kyushu, southern Japan. Eng Geol 108(1–2):1–15

Corominas J, Moya J, Ledesma A, Lloret A, Gili JA (2005) Prediction of ground displacements and velocities from groundwater level changes at the Vallcebre landslide (Eastern Pyrenees, Spain). Landslides 2:83–96

Crosta GB, Agliardi F (2002) How to obtain alert velocity thresholds for large rockslides. Phys Chem Earth. Parts A/B/C 27(36):1557–1565. doi:10.1016/S1474-7065(02)00177-8

Crosta GB, Chen H, Frattini P (2006) Forecasting hazard scenarios and implications for the evaluation of countermeasure efficiency for large debris avalanches. Eng Geol 83(1–3):236–253

Crosta GB, Agliardi F (2003) Failure forecast for large rock slides by surface displacement measurements. Can Geotech J 40:176–191

Crosta GB, Castellanza R, Frattini P, Broccolato M, Bertolo D, Cancelli P, Tamburini A (2012a) Comprehensive understanding of a rapid moving rockslide: the Mt de la Saxe landslide. MIR 2012 XIV Ciclo di Conferenze di Meccanica e Ingegneria delle Rocce—Nuovi metodi di indagine, monitoraggio e modellazione degli ammassi rocciosi, 20 pp

Crosta et al. (2012b) Caratterizzazione geologica, geofisica e geomeccanica del versante sinistro dell'invaso di Pian Palù—Monte Le Mandriole (Pejo,Ttn). relazione geologica-geomeccanica. (unpublished), 347 pp

Crosta G, Frattini P, Basiricò S, Cancelli P, Alberto W, Tamburini A (2011) Modello idrogeologico del versante di Mont de La Saxe e aggiornamento dello stato delle conoscenze. Regione Valle d'Aosta (unpublished report), 102 pp

De Giusti F, Bonetto F, Dal Piaz GV (2005) Carta geologica della Valle d'Aosta, scala 1:100.000. Regione Autonoma Valle d'Aosta, Assessorato territorio, ambiente e opere pubbliche

di Prisco C, Imposimato S (1996) Time dependent mechanical behaviour of loose sands. Mech Cohes-Frict Mater 1(1):45–73

di Prisco C, Zambelli C (2003) Cyclic and dynamic mechanical behaviour of granular soils: experimental evidence and constitutive modelling. Rev Franç Genie Civil 7(7–8):881–910

Eberhardt E, Watson AD, Loew S (2008) Improving the interpretation of slope monitoring and early warning data through better understanding of complex deep-seated landslide failure mechanisms. In: Chen Z, Zhang J, Li Z, Wu F, Ho K (Eds). Landslides and engineered slopes: from the past to the future, 10th Int. Symp. on Landslides and Engineered Slopes. Taylor & Francis, Xi'an, 39–51

Faulkner DR, Jackson CAL, Lunn RJ, Schlische RW, Shipton ZK, Wibberley CAJ, Withjack MO (2010) A review of recent developments concerning the structure, mechanics and fluid flow properties of fault zones. J Struct Geol 32:1557–1575

Fischer U, Kulli B, Flühler H (1998) Constitutive relationships and pore structure of undisturbed fracture zone samples with cohesionless fault gouge layers. Water Resour Res 34(7):1695–1701

Frigerio G (2010) Evoluzione di movimenti franosi lenti: interpretazione dei dati mediante modellazione numerica semplificata. Master thesis (in Italian), Politecnico di Milano

Ganerød GV, Grøneng G, Rønning JS, Dalsegg E, Elvebakk H, Tønnesen JF, Kveldsvik V, Eiken T, Blikra LH, Braathen A (2008) Geological model of the Åknes rockslide, western Norway. Eng Geol. doi:10.1016/j.enggeo.2008.01.018

Gillon MD, Hancox GT (1992) Cromwell gorge landslides: a general overview. In: Bell DH (ed). Landslides—Proceedings of the Sixth International Symposium, Christchurch, 10–14 February 1992, Rotterdam, A.A. Balkema, 1(3):83–102

Gillon MD, Riley PB, Lilley PB, Halliday GS (1992) Movement history and infiltration: Cairnmuir landslide. In: Bell DH (ed). Landslides—Proceedings of the Sixth International Symposium, Christchurch, 10–14 February 1992, Rotterdam, A.A. Balkema, 1(3): 103–109

Gischig VS, Moore JR, Evans KF, Amann F, Loew S (2011) Thermomechanical forcing of deep rock slope deformation: 2. The Randa rock slope instability. J Geophys Res Earth Surf 116(4):F0401

Glastonbury J, Fell R (2010) Geotechnical characteristics of large rapid rock slides. Can Geotech J 47(1):116–132. doi:10.1139/T09-080

Gleeson T, Manning AH (2008) Regional groundwater flow in mountainous terrain: three-dimensional simulations of topographic and hydrologeologic controls. Water Resour Res 44, W10403. doi:10.1029/2008WR006848

Gottardi G, Butterfield R (2001) Modelling ten years of downhill creep data. Proc. of the 15th Inter. Conf. on Soil Mechanics and Geotechnical Engineering. Istanbul, Turkey, 1–3, 27–31

Grøneng G, Christiansen HH, Nilsen B, Blikra LH (2011) Meteorological effects on seasonal displacements of the Åknes rockslide, western Norway. Landslides 8(1):1–15. doi:10.1007/s10346-010-0224-x

Guermani A, Pennacchioni G (1998) Brittle precursors of plastic deformation in a granite: an example from the Mont-Blanc massif (Helvetic, western Alps). J Struct Geol 20:135–148

Guglielmi Y, Cappa F, Binet S (2005) Coupling between hydrogeology and deformation of mountainous rock slopes: insights from La Clapière area (southern Alps, France). Compt Rendus Geosci 337:1154–1163

Original Paper

Helmstetter A, Garambois S (2010) Seismic monitoring of Séchilienne rockslide (French Alps): analysis of seismic signals and their correlation with rainfalls. J Geophys Res 115, F03016. doi:10.1029/2009JF001532

Karampatakis DA, Hatzigogos TN (1999) A model to describe creeping behavior of thin-layer element for interfaces and joints proceedings from COST C7 Workshop in Thessaloniki, 1–2 October 1999, 1–16

Kirsch R (2006) Petrophysical properties of permeable and low-permeable rocks. In: Kirsch R (ed) Groundwater geophysics. A tool for hydrogeology. Springer, Berlin. doi:10.1007/3-540-29387-6, 1–22

Lama RD, Vutukuri V (1978) Handbook on mechanical properties of rocks. Trans Tech Publ 2

Leloup PH, Arnaud N, Sobel ER, Lacassin R (2005) Alpine thermal and structural evolution of the highest external crystalline massif: the Mont Blanc. Tectonics 24, TC4002. doi:10.1029/2004TC001676

Lollino G, Arattano M, Allasia P, Giordan D (2006) Time response of a landslide to meteorological events. Nat Hazards Earth Syst Sci 6:179–184

Macfarlane DF (2009) Observations and predictions of the behaviour of large, slow-moving landslides in schist, Clyde Dam reservoir, New Zealand. Eng Geol 109(1–2):29, 5–15

Macfarlane DF, Riddolls BW, Crampton NA, Foley MR (1992a) Engineering geology of schist landslides, Cromwell, New Zealand. In: Bell DH (ed.). Landslides—Proceedings of the Sixth International Symposium, Christchurch, 10–14 February 1992, Rotterdam, A.A. Balkema, 3(3):2137–2144

Macfarlane DF, Pattle AD, Salt G (1992b) Nature and indentification of Cromwell Gorge landslides groundwater systems. In: Bell DH (ed.). Landslides—Proceedings of the Sixth International Symposium, Christchurch, 10–14 February 1992, Rotterdam, A.A. Balkema, 1(3):509–518

Mansour MF, Martin CD, Morgenstern NR (2011) Movement behaviour of the little chief slide. Can Geotech J 48(4):655–670

Moore DP, Imrie AS (1995) Stabilization of Dutchman's Ridge. In: Bell DH (ed.). International symposium on landslides. ISL VI. Balkema, Christchurch, pp. 1783–1788

Newmark NM (1965) Effects of earthquakes on dams and embankments. Geotechnique 15(2):139–160

Nishii R, Matsuoka N, Daimaru H, Yasuda M (2013) Precursors and triggers of an alpine rockslide in Japan: the 2004 partial collapse during a snow-melting period. Landslides 10:75–82. doi:10.1007/s10346-012-0353-5

Palmstrom A (1995) RMi—a rock mass characterization system for rock engineering purposes. PhD thesis, Oslo Univ., 400 pp

Perello P, Piana F, Martinotti G (1999) Neo-Alpine structural features at the boundary between the Penninic and Helvetic domains (Prè S. Didier-Entrèves, Aosta valley, Italy). Eclogae Geol Helv 92:347–359

Perzyna P (1963) The constitutive equations for rate sensitive plastic materials. Quart Appl Math 20:321–332

Pisani G, Castelli M, Scavia C (2010) Hydrogeological model and hydraulic behaviour of a large landslide in the Italian Western Alps. Nat Hazards Earth Syst Sci 10:2391–2406

Puzrin AM, Schmid A (2012) Evolution of stabilized creeping landslides. Geotechnique 62(6):491–501

Ranalli M, Gottardi G, Medina-Cetina Z, Nadim F (2010) Uncertainty quantification in the calibration of a dynamic viscoplastic model of slow slope movements. Landslides 7:31–41

Ratto S, Giardino M, Giordan D, Alberto W, Armand M (2007) Carta dei fenomeni franosi della valle d'Aosta, 1:100 000 in scale. Tipografia valdostana, Aosta

Riedmüller G, Brosch FJ, Klima K, Medley EW (2001) Engineering geological characterization of brittle faults and classification of fault rocks. Felsbau 19(4):13–19

Sausgruber T, Brandner R (2003) The relevance of brittle fault zones in tunnel construction—Lower Inn Valley Feeder Line North of the Brenner Base Tunnel, Tyrol, Austria. Mitt Österr Geol Ges 0251–7493(94):157–172

Secondi M, Crosta GB, di Prisco C, Frigerio G, Frattini P, Agliardi F (2013) Landslide motion forecasting by a dynamic visco-plastic model. In Landslide Science and Practice, Volume 3: Spatial Analysis and Modelling; Eds. Margottini C, Canuti P, Sassa K, Springer, 151–159

Sjögren B, Øvsthus A, Sandberg L (1979) Seismic classification of rock mass qualities. Geophys Prospect 27(2):409–442

Zangerl C, Eberhardt E, Perzlmaier S (2010) Kinematic behaviour and velocity characteristics of a complex deep-seated crystalline rockslide system in relation to its interaction with a dam reservoir. 112(1IN)53 1I

Watkins JS, Walters LA, Godson RH (1972) Dependence of in-situ compressional-wave velocity on porosity in unsaturated rocks. Geophysics 37(1):29–35

Wyllie MRJ, Gregory AR, Gardner LW (1956) Elastic wave velocities in heterogeneous and porous media. Geophysics 21:41–70

Wyllie MRJ, Gregory AR, Gardner LW (1958) An experimental investigation of factors affecting elastic wave velocities in porous media. Geophysics 23:459–493

G. B. Crosta (✉) · **P. Frattini** · **G. Frigerio** · **R. Castellanza** · **F. Agliardi**
Department Earth and Environmental Sciences,
Univ. degli Studi di Milano Bicocca,
Piazza della Scienza 4, 20126, Milan, Italy
e-mail: giovannibattista.crosta@unimib.it

C. di Prisco
Department of Structural Engineering,
Politecnico di Milano,
Milan, Italy